

Kaon T-even transverse-momentum-dependent distributions and form factors in a self-consistent light-front quark model

Yongwoo Choi,^{1, 2, *} Ahmad Jafar Arifi,^{3, 4, †} Ho-Meoyng Choi,^{5, ‡} and Chueng-Ryong Ji^{6, §}

¹*Institute of Quantum Science, Inha University, Incheon 22212, Republic of Korea*

²*The Center for High Energy Physics, Kyungpook National University, Daegu 41566, Republic of Korea*

³*Research Center for Nuclear Physics (RCNP), The University of Osaka, Ibaraki 567-0047, Japan*

⁴*Advanced Science Research Center, Japan Atomic Energy Agency (JAEA), Ibaraki 319-1195, Japan*

⁵*Department of Physics Education, Teachers College,*

Kyungpook National University, Daegu 41566, Republic of Korea

⁶*Department of Physics and Astronomy, North Carolina State University, Raleigh, NC 27695-8202, USA*

(Dated: December 29, 2025)

We present a self-consistent light-front quark model (LFQM) for the kaon based on the Bakamjian–Thomas (BT) construction and apply it to the electromagnetic and scalar form factors, as well as the full set of unpolarized T-even transverse-momentum-dependent distributions (TMDs) and their collinear parton distribution functions (PDFs). A uniform use of the invariant mass M_0 in both hadronic matrix elements and Lorentz prefactors enforces four-momentum conservation at the meson–quark vertex and yields current-component-independent observables, removing light-front zero-mode ambiguities. Properly normalized electromagnetic form factor $F_{K+}(Q^2)$ is exemplified as a current-component-independent observable by verifying its uniqueness with the explicit computation from all the available components (γ^+ , γ^\perp , and γ^-) of the current. In the scalar channel, we compare the direct $f_S(Q^2)$ and mass-factored $F_S(Q^2)$ definitions and show they are not interchangeable within the BT-based LFQM because $M \rightarrow M_0(x, \mathbf{k}_\perp)$ must be implemented inside the integral. Using a Gaussian form for the light-front wave function, the twist-2 TMD f_1^q becomes exactly Gaussian in \mathbf{k}_\perp , while higher-twist TMDs ($f^{\perp q}$, e^q , f_4^q) display systematic twist/flavor hierarchies, including an elliptic deformation of f_4^q tied to γ^- component. The BT-based LFQM satisfies the forward-limit sum rule for $f_4^q(x)$. We further analyze the perturbative QCD evolution of the valence PDFs for the pion and kaon and report their Mellin moments at representative scales, enabling direct comparison with phenomenology. Overall, the BT-based LFQM provides a unified, current-independent description of meson structure and a consistent bridge from nonperturbative light-front dynamics to evolved collinear PDFs.

I. INTRODUCTION

Exploring the quark–gluon substructure of light mesons is a longstanding challenge in hadron physics, offering crucial tests of our understanding of QCD in the nonperturbative regime. The kaon, like the pion, is a Nambu–Goldstone boson arising from spontaneous chiral-symmetry breaking, and both share a simple valence quark–antiquark composition. However, unlike the pion, the kaon contains a strange quark, introducing explicit SU(3) flavor-symmetry breaking due to the large mass difference between the strange and light quarks. This difference introduces a heavier mass scale, modifies its internal momentum distributions, and makes the kaon a unique laboratory for studying how flavor-symmetry breaking influences hadronic structure.

While pion and kaon observables—such as decay constants, distribution amplitudes (DAs) [1–5], electromagnetic form factors (EMFFs) [6–10], parton distribution functions (PDFs) [11–18] and generalized parton dis-

tributions (GPDs) [19–26]—have been extensively studied, their transverse-momentum-dependent distributions (TMDs) [27–31] remain comparatively less developed. In particular, kaon studies are generally less advanced than those for the pion, with TMDs being especially under-explored. Extending such analyses to the kaon provides complementary insight into the spatial and momentum distributions of its quark constituents and offers a more complete picture of nonperturbative QCD dynamics.

TMDs [32–34] extend the concept of collinear PDFs by incorporating the intrinsic transverse momentum \mathbf{k}_\perp of partons, thereby offering a three-dimensional description of hadrons in momentum space [35–38]. They encode information not only on the longitudinal momentum fraction x of partons but also on correlations between \mathbf{k}_\perp and the spin of the hadron or the parton itself. Experimental progress in semi-inclusive deep inelastic scattering (SIDIS) [39], Drell–Yan (DY) processes [32, 40], and high-energy hadron collisions at the LHC has significantly advanced our knowledge of TMDs. The upcoming Electron-Ion Collider (EIC) [41] and other planned facilities, such as the EicC [42] and COMPASS++/AMBER [43], promise to deliver precision data over broad kinematic regimes, enabling deeper exploration of the partonic structure of mesons and baryons.

Despite these developments, experimental data on the kaon’s parton structure remain scarce. At present, the

* sunctchoi@gmail.com

† aj.arifi01@gmail.com

‡ homyoung@knu.ac.kr

§ crji@ncsu.edu

only direct constraint comes from the valence-quark ratio u^π/u^K measured by the NA23 Collaboration [44]. Recent proposals suggest exploiting J/ψ production in kaon-induced processes to extract additional information [45, 46]. Lattice QCD has also begun providing calculations of meson PDFs [47–55], DAs, and other observables from the first-principles, offering valuable theoretical inputs. These efforts, together with future experimental programs, are expected to significantly enhance our understanding of the kaon’s structure.

Among the various theoretical approaches used to study hadron structure, the light-front quark model (LFQM) [56, 57], formulated in light-front dynamics (LFD), offers distinct advantages, enabling a direct partonic interpretation of various parton distribution observables, including DAs, PDFs, GPDs, TMDs, and their unified representation through generalized transverse-momentum-dependent distributions, all of which can be expressed in terms of light-front wave functions (LFWFs).

In the light-front (LF) formalism, TMDs can be related to the EMFF through their representation in terms of hadronic matrix elements of bilinear quark-field correlators. As shown in Refs. [27, 28], unpolarized TMDs — at both leading and higher twist — can be formulated in the LFQM. In this approach, four T-even unpolarized TMDs, $\{f_1^q(x, \mathbf{k}_\perp), f_3^q(x, \mathbf{k}_\perp), f_4^q(x, \mathbf{k}_\perp), e^q(x, \mathbf{k}_\perp)\}$ form a complete set for unpolarized targets, with a Lorentz-invariance relation among them holding in the absence of explicit gauge degrees of freedom. Of these, $\{f_1^q(x, \mathbf{k}_\perp), f_3^q(x, \mathbf{k}_\perp), f_4^q(x, \mathbf{k}_\perp)\}$ are directly linked to the forward matrix elements of the electromagnetic (EM) vector current $\langle h|\bar{\psi}(0)\gamma^\mu\psi(0)|h\rangle$, with $\mu = +, \perp$, and $-$ corresponding to twist-2, twist-3, and twist-4 TMDs, respectively. Since these TMDs are related to the EMFF through specific current components, an extraction of the EMFF that is independent of the chosen current component is essential for obtaining physically consistent TMDs. The remaining one, $e^q(x, \mathbf{k}_\perp)$, is the twist-3 TMD associated with the matrix element of the scalar current $\bar{\psi}\psi$. Importantly, higher-twist TMDs such as f_3^q and e^q play a non-negligible role in DY observables [28, 32], making their study essential for a complete understanding of quark dynamics beyond the leading-twist picture.

However, Refs. [27, 28] noted the difficulties in computing the twist-4 quark TMD $f_4^q(x, \mathbf{k}_\perp)$, which corresponds to the minus component of the vector current, and in satisfying the sum rule for its twist-4 PDF $f_4^q(x)$. While the twist-4 TMD is hard to access experimentally, its correct extraction is very important to check the self-consistency of the model. This issue is closely tied to the LF zero-mode problem [58–61] arising from the use of the “bad” (minus) component of the current. In a recent LFQM analysis [62] for the pion EMFF and the three TMDs $\{f_1^q(x, \mathbf{k}_\perp), f_3^q(x, \mathbf{k}_\perp), f_4^q(x, \mathbf{k}_\perp)\}$, two of us resolved the LF zero-mode issue associated with the minus component of the current and provided the current-component

independent predictions for both the EMFF and these TMDs.

This resolution was achieved within our self-consistent LFQM [62–70], formulated to ensure that physical observables are extracted in a current-component-independent manner. The model is built upon the Bakamjian–Thomas (BT) construction [71–73], which incorporates interactions while preserving relativistic consistency. In this framework, meson states are composed of free, on-mass-shell quark–antiquark pairs, with interactions introduced through the Casimir mass operator, $M = M_0 + V_{q\bar{q}}$, as demonstrated in our extensive mass-spectroscopic studies of pseudoscalar and vector mesons, including both ground and radially excited states [74–79].

When evaluating the hadronic matrix element of a local current \mathcal{O}^μ within the BT-based LFQM,

$$\langle P'|\mathcal{O}^\mu|P\rangle = \mathcal{P}^\mu \mathcal{F}, \quad (1)$$

where \mathcal{F} denotes the physical observable (e.g., a decay constant or a form factor) and \mathcal{P}^μ encodes the Lorentz structure, the on-shell condition at the meson–quark vertex enforces overall four-momentum conservation, $P = p_q + p_{\bar{q}}$. In particular, LF energy conservation, $P^- = p_q^- + p_{\bar{q}}^-$, identifies the physical meson mass M with the invariant mass M_0 constructed from the constituent momenta. This in turn requires the replacement $M \rightarrow M_0$ at the meson–quark vertex, yielding the consistency condition

$$\frac{M_0^2 + \mathbf{P}_\perp^2}{P^+} = \frac{m_q^2 + \mathbf{p}_{q\perp}^2}{p_q^+} + \frac{m_{\bar{q}}^2 + \mathbf{p}_{\bar{q}\perp}^2}{p_{\bar{q}}^+}. \quad (2)$$

While the matrix element $\langle P'|\mathcal{O}^\mu|P\rangle$ in Eq. (1) is naturally expressed in terms of M_0 within this framework, the Lorentz structure \mathcal{P}^μ used to extract \mathcal{F} may still be evaluated using the physical mass M , for example through the minus components P^- and P'^- that enter the construction of \mathcal{P}^μ .

As in many earlier LFQM calculations (see, e.g., Refs. [80, 81]), if M is retained in \mathcal{P}^μ without implementing the replacement $M \rightarrow M_0$, an inconsistency arises between the two sides of Eq. (1), which manifests as the familiar LF zero-mode problem. We refer to this scheme as the partially BT-implemented LFQM, in which the BT construction is applied to the matrix elements but not to the Lorentz structure.

To resolve this inconsistency, we have proposed [62–69] a self-consistent formulation that applies the BT construction uniformly to both the hadronic matrix elements and the Lorentz structures. In this approach, the physical observable is computed as

$$\mathcal{F} = \langle P'|\frac{\mathcal{O}^\mu}{\mathcal{P}^\mu}|P\rangle_{\text{BT}}, \quad (3)$$

where the subscript “BT” indicates that the entire expression is evaluated with the BT construction, and \mathcal{P}^μ

is incorporated consistently into the integral. This unified treatment ensures that \mathcal{F} is independent of the choice of current component and free from zero-mode contamination. In this sense, the replacement $M \rightarrow M_0$ is not merely a technical simplification but a defining feature of the BT-based LFQM, essential for obtaining current-component-independent results.

Hereafter, we refer to our self-consistent BT-based formulation as the full BT-based (fBT) LFQM and to the partially BT-implemented scheme as the partial BT-based (pBT) LFQM.

The main goal of this work is to extend our fBT-LFQM analysis on the pion [62] to the kaon. In doing so, we incorporate the twist-3 TMD associated with the scalar-current matrix element, thereby enabling a complete analysis of the four T-even unpolarized TMDs.

The paper is organized as follows. Section II reviews our LFQM and its BT-based implementation. Section III presents the EM and scalar form factors of pseudoscalar mesons, contrasts the fBT-LFQM with the pBT-LFQM, and discusses possible LF zero-mode contributions associated with the $(-)$ component of the vector current as well as with the scalar channel. Section IV defines the TMDs and PDFs at various twists, relates them to forward matrix elements in the vector and scalar channels, and compares with existing formulations in the literature. Section V presents numerical results for the unpolarized T-even TMDs and PDFs at the model scale μ_0 , and performs NNLO DGLAP evolution of the twist-2 PDFs for comparison with other approaches. Section VI summarizes our findings. Appendix A derives the relation between the TMD correlator and the forward matrix elements in the vector and scalar channels.

II. MODEL DESCRIPTION

Our fBT-LFQM for $q\bar{q}$ bound-state mesons with total momentum P describes the meson as a Fock state of non-interacting constituent quark q and antiquark \bar{q} , with interaction effects incorporated through the mass operator $M = M_0 + V_{q\bar{q}}$ [74–79], that is the Casimir operator commuting with all other Poincaré operators. Thus, this formulation preserves the Poincaré algebra for the two-particle bound-state system. The interaction dynamics are encoded in the LFWF which is the eigenfunction of the mass operator.

The four-momentum P of a meson in LF coordinates is expressed as $P = (P^+, P^-, \mathbf{P}_\perp)$, where $P^+ = P^0 + P^3$ represents the longitudinal LF momentum, $P^- = P^0 - P^3$ corresponds to the LF energy, and $\mathbf{P}_\perp = (P^1, P^2)$ denotes the transverse momentum components. We adopt the Minkowski metric convention, in which the inner product of two four-vectors is defined as $a \cdot b = \frac{1}{2}(a^+b^- + a^-b^+) - \mathbf{a}_\perp \cdot \mathbf{b}_\perp$.

The meson state $|P\rangle$ with momentum P and total an-

gular momentum (J, J_z) is constructed as

$$|P\rangle = \int [d^3\mathbf{p}_1] [d^3\mathbf{p}_2] 2(2\pi)^3 \delta^3(\mathbf{P} - \mathbf{p}_1 - \mathbf{p}_2) \sum_{\lambda_1, \lambda_2} \Psi_{\lambda_1 \lambda_2}^{J, J_z}(\mathbf{p}_1, \mathbf{p}_2) |q(p_1, \lambda_1)\bar{q}(p_2, \lambda_2)\rangle, \quad (4)$$

where $p_{1(2)}$ are the four-momenta and $\lambda_{1(2)}$ the helicities of the on-shell constituent quark and antiquark, respectively. The LF three-momentum is $\mathbf{p} = (p^+, \mathbf{p}_\perp)$ and the integration measure is $[d^3\mathbf{p}] = \frac{dp^+ d^2\mathbf{p}_\perp}{2(2\pi)^3}$.

The model wave function of pseudoscalar meson ($J = 0, J_z = 0$) is denoted by $\Psi_{\lambda_1 \lambda_2}^{00}(x, \mathbf{k}_\perp)$ as exemplified in the following description. The LF relative momentum variables (x, \mathbf{k}_\perp) are defined as $x_i = p_i^+/P^+$ and $\mathbf{k}_{i\perp} = \mathbf{p}_{i\perp} - x_i \mathbf{P}_\perp$, satisfying the momentum conservation conditions $\sum_i x_i = 1$ and $\sum_i \mathbf{k}_{i\perp} = 0$. In this work, we set $x_1 \equiv x$ and $\mathbf{k}_{1\perp} \equiv \mathbf{k}_\perp$.

Normalizing the state $|P\rangle$ as [69]

$$\langle P' | P \rangle = 2(2\pi)^3 P^+ \delta^{(3)}(\mathbf{P}' - \mathbf{P}), \quad (5)$$

the corresponding LFWF normalization condition reads

$$\int_0^1 dx \int \frac{d^2\mathbf{k}_\perp}{2(2\pi)^3} \sum_{\lambda_1 \lambda_2} \Psi_{\lambda_1 \lambda_2}^{\dagger 00}(x, \mathbf{k}_\perp) \Psi_{\lambda_1 \lambda_2}^{00}(x, \mathbf{k}_\perp) = 1. \quad (6)$$

The model wave function is written as

$$\Psi_{\lambda_1 \lambda_2}^{00}(x, \mathbf{k}_\perp) = \phi(x, \mathbf{k}_\perp) \mathcal{R}_{\lambda_1 \lambda_2}^{00}(x, \mathbf{k}_\perp), \quad (7)$$

where $\phi(x, \mathbf{k}_\perp)$ is the radial wave function and $\mathcal{R}_{\lambda_1 \lambda_2}^{00}$ denotes the spin-orbit wave function obtained via the interaction-independent Melosh transformation [82].

The covariant form of $\mathcal{R}_{\lambda_1 \lambda_2}^{00}$ is given by [80, 81]

$$\mathcal{R}_{\lambda_1 \lambda_2}^{00} = \frac{\bar{u}_{\lambda_1}(p_1) \gamma_5 v_{\lambda_2}(p_2)}{\sqrt{2} \sqrt{M_0^2 - (m_1 - m_2)^2}}, \quad (8)$$

where $m_{1(2)}$ is the mass of quark (antiquark), and

$$M_0^2 = \frac{\mathbf{k}_\perp^2 + m_1^2}{x} + \frac{\mathbf{k}_\perp^2 + m_2^2}{1-x}, \quad (9)$$

is the invariant mass squared of the $q\bar{q}$ system.

By explicitly evaluating the above covariant expression with Dirac spinors [56, 80, 81], one obtains the matrix representation of $\mathcal{R}_{\lambda_1 \lambda_2}^{00}$ in terms of (x, \mathbf{k}_\perp) as

$$\mathcal{R}_{\lambda_1 \lambda_2}^{00} = \frac{1}{\sqrt{2} \sqrt{\mathcal{A}^2 + \mathbf{k}_\perp^2}} \begin{pmatrix} -k^L & \mathcal{A} \\ -\mathcal{A} & -k^R \end{pmatrix}, \quad (10)$$

where $k^{R(L)} = k_x \pm ik_y$ and $\mathcal{A} = (1-x)m_1 + xm_2$. We note that $\mathcal{R}_{\lambda_1 \lambda_2}^{00}$ automatically satisfies the unitarity condition $\sum_{\lambda_1, \lambda_2} \mathcal{R}_{\lambda_1 \lambda_2}^{00\dagger} \mathcal{R}_{\lambda_1 \lambda_2}^{00} = 1$.

The form of Eq. (9) arises from enforcing the on-mass-shell conditions for the constituent quark and antiquark

together with LF energy conservation at the meson-quark vertex, $P^- = p_1^- + p_2^-$. This leads to the relation between x and the z -component k_z of the quark's three-momentum [80, 81]:

$$k_z = \left(x - \frac{1}{2} \right) M_0 + \frac{(m_2^2 - m_1^2)}{2M_0}, \quad (11)$$

from which the Jacobian factor for the transformation $(x, \mathbf{k}_\perp) \rightarrow (k_z, \mathbf{k}_\perp)$ is

$$\frac{\partial k_z}{\partial x} = \frac{M_0}{4x(1-x)} \left[1 - \frac{(m_1^2 - m_2^2)^2}{M_0^4} \right]. \quad (12)$$

The quark-antiquark interaction is incorporated through the mass operator [71–73] $M = M_0 + V_{q\bar{q}}$, whose eigenvalues yield the meson mass spectrum. In our BT-based LFQM, the radial wave function $\phi(x, \mathbf{k}_\perp)$ is treated as a variational trial function, optimized for a QCD-motivated effective Hamiltonian, $H_{q\bar{q}} |\Psi\rangle = (M_0 + V_{q\bar{q}}) |\Psi\rangle = M_{q\bar{q}} |\Psi\rangle$, where $M_{q\bar{q}}$ denotes the $q\bar{q}$ meson mass eigenvalue. Comprehensive meson spectroscopy analyses in this approach are reported in Refs. [74–79].

For the $1S$ meson state, we adopt a Gaussian form:

$$\phi(x, \mathbf{k}_\perp) = \frac{4\pi^{3/4}}{\beta^{3/2}} \sqrt{\frac{\partial k_z}{\partial x}} \exp\left(-\frac{\mathbf{k}^2}{2\beta^2}\right), \quad (13)$$

where $\mathbf{k}^2 = \mathbf{k}_\perp^2 + k_z^2$, and β is a variational parameter fixed from mass spectrum fits [74–79]. The state normalization in Eq. (5), together with the unitarity of the spin-orbit wave function, ensures that ϕ satisfies

$$\int_0^1 dx \int \frac{d^2 \mathbf{k}_\perp}{2(2\pi)^3} |\phi(x, \mathbf{k}_\perp)|^2 = 1. \quad (14)$$

In our numerical analysis for the pseudoscalar mesons, we employ the model parameters determined within the linear confining potential model [74]. The model parameters are given by

$$(m_q, m_s, \beta_{q\bar{q}}, \beta_{q\bar{s}}) = (0.22, 0.45, 0.3659, 0.3886) \text{ GeV}, \quad (15)$$

where $q = u = d$ is assumed under SU(2) flavor symmetry. The parameters $(m_q, \beta_{q\bar{q}})$ correspond to the pion ($\pi^+ = u\bar{d}$), while $(m_q, m_s, \beta_{q\bar{s}})$ are used for the kaons ($K^+ = u\bar{s}$ and $K^0 = d\bar{s}$). These parameter sets provide reasonable descriptions of the ground-state pseudoscalar mesons. For the pion, the model predicts the charge radius and decay constant as $\langle r_{\pi^+}^2 \rangle^{1/2} = 0.654$ fm and $f_\pi = 130$ MeV, which are consistent with the experimental values of (0.659 ± 0.004) fm and 131 MeV, respectively [83]. For the kaon, the predictions are $\langle r_{K^+}^2 \rangle^{1/2} = 0.595$ fm and $f_K = 161$ MeV, in reasonable agreement with the experimental data of (0.560 ± 0.031) fm and (155.7 ± 0.3) MeV, respectively [83].

III. ELECTROMAGNETIC AND SCALAR FORM FACTORS

A. Comparison of fBT-LFQM and pBT-LFQM

Before describing EMFFs, we outline the formalism describing weak transitions between two pseudoscalar mesons, specifically the process in which an initial meson with momentum P and mass M transitions to a final meson with momentum P' and mass M' . The four-momentum transfer is defined as $q = P' - P$. The corresponding weak-current matrix element admits the covariant decomposition

$$\begin{aligned} \langle \mathcal{J}_W^\mu \rangle &\equiv \langle P' | \bar{q}(0) \gamma^\mu (1 - \gamma_5) q(0) | P \rangle \\ &= \left(\bar{P}^\mu - q^\mu \frac{\bar{P} \cdot q}{q^2} \right) F(q^2) + q^\mu \frac{\bar{P} \cdot q}{q^2} H(q^2), \end{aligned} \quad (16)$$

where $\bar{P} = P + P'$ and $\bar{P} \cdot q = M'^2 - M^2$. The Lorentz structure multiplying $F(q^2)$ is transverse to q^μ and therefore gauge invariant, while the term multiplying $H(q^2)$ is longitudinal; it vanishes for conserved currents (e.g. EM current) and contributes only when the current is not conserved.

In the EM transition for a pseudoscalar meson, current conservation ($q_\mu \langle J_{\text{em}}^\mu \rangle = 0$) alone is sufficient to eliminate the longitudinal structure: contracting Eq. (16) with q_μ gives $q_\mu \langle \mathcal{J}_{\text{em}}^\mu \rangle = (\bar{P} \cdot q) H(q^2)$. Hence, for a conserved current one must have $H(q^2) = 0$ irrespective of the value of $\bar{P} \cdot q$. In particular, within the fBT-LFQM the Lorentz prefactor is built with the invariant masses M_0 and M'_0 constructed from internal momenta, so even for an elastic EM process ($M = M'$) one has $\bar{P} \cdot q = M'^2 - M_0^2 \neq 0$ point-by-point in the integrand. After integration, however, current conservation enforces transversality of the full matrix element and only the gauge-invariant term survives:

$$\begin{aligned} \langle \mathcal{J}_{\text{em}}^\mu \rangle &\equiv \langle P' | \bar{q}(0) \gamma^\mu q(0) | P \rangle \\ &= \left(\bar{P}^\mu - q^\mu \frac{\bar{P} \cdot q}{q^2} \right) F_V(Q^2). \end{aligned} \quad (17)$$

where $Q^2 = -q^2$.

For the analysis of the twist-3 TMD $e^q(x, \mathbf{k}_\perp)$ associated with the scalar current, and to maintain consistency with its definition, we also study the scalar form factor of a pseudoscalar meson. We adopt two standard conventions:

(A) Direct (no-prefactor) convention [84–87]:

$$\langle P' | \bar{q}(0) \mathbf{1} q(0) | P \rangle = f_S(Q^2). \quad (18)$$

(B) Mass-factored (nucleon-like) convention [88–90]—commonly used when extracting the twist-3 TMD $e^q(x, \mathbf{k}_\perp)$, e.g. [27, 28]:

$$\langle P' | \bar{q}(0) \mathbf{1} q(0) | P \rangle \equiv 2M F_S(Q^2). \quad (19)$$

At the level of definitions, the two are related by $f_S(Q^2) = 2M F_S(Q^2)$. Accordingly, they seem to

be interchangeable. In our fBT-LFQM, however, the Lorentz prefactor is implemented under the (x, \mathbf{k}_\perp) integral via $M \rightarrow M_0(x, \mathbf{k}_\perp)$, so the naive identification $F_S = f_S/(2M)$ no longer holds. We defer the detailed implications for the e^q normalization to the TMD analysis in Sec. IV.

The calculations of the hadronic matrix elements for the EM vector and scalar currents, $\langle P'|\bar{q}(0)\Gamma q(0)|P\rangle$ with $\Gamma \in \{\gamma^\mu, \mathbf{1}\}$, are performed identically in both the fBT-LFQM and the pBT-LFQM, since in both schemes the BT construction is applied to the matrix element itself. The essential difference between them lies in the treatment of the Lorentz prefactors. In the pBT-LFQM one retains the physical masses (with $M = M'$ for elastic EM kinematics) in the prefactors, whereas in the fBT-LFQM the BT construction is applied uniformly to both the matrix element and the Lorentz prefactor to ensure consistency.

In the pBT-LFQM, the form factor is extracted as

$$F_{\text{pBT}}^{[\Gamma]}(Q^2) = \frac{1}{\mathcal{P}_{\text{pBT}}^{[\Gamma]}} \langle P'|\bar{q}(0)\Gamma q(0)|P\rangle_{\text{BT}}, \quad (20)$$

with

$$\begin{aligned} \mathcal{P}_{\text{pBT}}^{[\gamma^\mu]} &= (P + P')^\mu, \\ \mathcal{P}_{\text{pBT}}^{[\mathbf{1}]} &= 2M. \end{aligned} \quad (21)$$

By contrast, in the fBT-LFQM we extract

$$F_{\text{fBT}}^{[\Gamma]}(Q^2) = \langle P'|\frac{\bar{q}(0)\Gamma q(0)}{\mathcal{P}_{\text{fBT}}^{[\Gamma]}}|P\rangle_{\text{BT}}, \quad (22)$$

with the covariant prefactor

$$\begin{aligned} \mathcal{P}_{\text{fBT}}^{[\gamma^\mu]} &= \bar{P}^\mu - q^\mu \frac{\bar{P} \cdot q}{q^2}, \\ \mathcal{P}_{\text{fBT}}^{[\mathbf{1}]} &= 2M_0, \end{aligned} \quad (23)$$

and the BT replacements $M \rightarrow M_0(x, \mathbf{k}_\perp)$ and $M' \rightarrow M_0(x, \mathbf{k}'_\perp)$ made inside the (x, \mathbf{k}_\perp) integration for both the matrix element and the prefactor. This uniform application removes the mismatch between left- and right-hand sides and eliminates zero-mode contamination, yielding current-component-independent results.

B. Form Factors in the BT-based LFQM Framework

To compute the EMFF and scalar form factor, we adopt the Drell–Yan–West ($q^+ = 0$) frame with $\mathbf{P}_\perp = 0$, in which $q^2 = -\mathbf{q}_\perp^2 \equiv -Q^2$. In this frame, the four-momenta of the initial and final meson states are

$$\begin{aligned} P &= \left(P^+, \frac{M^2}{P^+}, 0_\perp \right), \\ P' &= \left(P^+, \frac{M'^2 + \mathbf{q}_\perp^2}{P^+}, \mathbf{q}_\perp \right), \\ q &= \left(0, \frac{M'^2 - M^2 + \mathbf{q}_\perp^2}{P^+}, \mathbf{q}_\perp \right). \end{aligned} \quad (24)$$

The LF on-shell momenta $p_{1(2)}$ of the incoming quark (antiquark) and $p'_{1(2)}$ of the outgoing quark (antiquark) for the transition $|P(q\bar{q})\rangle \rightarrow |P'(q'\bar{q}')\rangle$ are given by

$$\begin{aligned} p_i^+ &= p_i'^+ = x_i P^+, \\ \mathbf{p}_{i\perp} &= x_i \mathbf{P}_\perp + \mathbf{k}_{i\perp}, \quad \mathbf{p}'_{i\perp} = x_i \mathbf{P}'_\perp + \mathbf{k}'_{i\perp}, \end{aligned} \quad (25)$$

where $x_1 = x$ and $\mathbf{k}_{1\perp} = \mathbf{k}_\perp$. Since the spectator antiquark ($i = 2$) satisfies $p_2^+ = p_2'^+$ and $\mathbf{p}_{2\perp} = \mathbf{p}'_{2\perp}$, it follows that $\mathbf{k}'_\perp = \mathbf{k}_\perp + (1 - x)\mathbf{q}_\perp$.

In both BT-based LFQMs, which employ a noninteracting $q\bar{q}$ representation, the one-loop contribution to the matrix elements of the vector and scalar currents is obtained by convoluting the initial and final state LFWFs [62]:

$$\langle P'|\bar{q}(0)\Gamma q(0)|P\rangle_{\text{BT}} = \int [d^3\mathbf{k}] \phi'(x, \mathbf{k}'_\perp) \phi(x, \mathbf{k}_\perp) S^{[\Gamma]}, \quad (26)$$

where $[d^3\mathbf{k}] = \frac{dk^+ d^2\mathbf{k}_\perp}{2(2\pi)^3}$ and $S^{[\Gamma]}$ denotes the spin factors for the vector and scalar currents, given by

$$S^{[\Gamma]} = \mathcal{R}_{\lambda'_1 \lambda_2}^\dagger \left[\frac{\bar{u}_{\lambda'_1}(p'_1)}{\sqrt{p'_1^+}} \Gamma \frac{u_{\lambda_1}(p_1)}{\sqrt{p_1^+}} \right] \mathcal{R}_{\lambda_1 \lambda_2}, \quad (27)$$

with an implicit sum over quark helicities. The explicit Dirac matrix elements of the vector and scalar currents for helicity spinors are listed in Table I.

Table II summarizes the spin factors $S^{[\Gamma]}$ and the Lorentz prefactors $\mathcal{P}_{\text{pBT}}^{[\Gamma]}$ and $\mathcal{P}_{\text{fBT}}^{[\Gamma]}$ for all components of the vector current ($\Gamma = \gamma^\mu$) and for the scalar current ($\Gamma = \mathbf{1}$). In both BT-based LFQMs, the EM current matrix element is computed within the same BT construction using free on-shell quark propagators. As a result, the spin factor $S^{[\Gamma]}$ is identical in the two formulations. For $S^{[\gamma^\mu]}$, the γ^+ and γ^\perp components receive contributions only from helicity–nonflip terms, whereas the γ^- component contains both a helicity–nonflip term proportional to \mathcal{B} and a helicity–flip term proportional to \mathcal{A} .

The EMFF ($\Gamma = \gamma^\mu$) and scalar FF ($\Gamma = \mathbf{1}$) in our fBT-LFQM are defined by

$$F_{\text{fBT}}^{[\Gamma]}(Q^2) = \int [d^3\mathbf{k}] \phi'(x, \mathbf{k}'_\perp) \phi(x, \mathbf{k}_\perp) \frac{S^{[\Gamma]}}{\mathcal{P}_{\text{fBT}}^{[\Gamma]}}, \quad (28)$$

where all occurrences of the meson masses $M^{(\prime)}$ in $\mathcal{P}_{\text{fBT}}^{[\Gamma]}$ of Table II are replaced by the corresponding invariant masses $M_0^{(\prime)}$, with $M_0' = M_0(x, \mathbf{k}'_\perp)$. For the EMFF calculation, we find that all three current components yield identical results, confirming the self-consistency of the fBT-LFQM: $F_{\text{fBT}}^{[\gamma^+]} = F_{\text{fBT}}^{[\gamma^\perp]} = F_{\text{fBT}}^{[\gamma^-]}$.

By contrast, in the pBT-LFQM the EMFF is obtained as

$$F_{\text{pBT}}^{[\Gamma]}(Q^2) = \frac{1}{\mathcal{P}_{\text{pBT}}^{[\Gamma]}} \int [d^3\mathbf{k}] \phi'(x, \mathbf{k}'_\perp) \phi(x, \mathbf{k}_\perp) S^{[\Gamma]}, \quad (29)$$

TABLE I. Dirac matrix elements for the helicity spinors. Note that $p^{L(R)}q^{R(L)} = \mathbf{p}_\perp \cdot \mathbf{q}_\perp \pm i\mathbf{p}_\perp \times \mathbf{q}_\perp$.

		Helicity ($\lambda \rightarrow \lambda'$)	
Matrix elements		$\uparrow \rightarrow \uparrow$	$\uparrow \rightarrow \downarrow$
		$\downarrow \rightarrow \downarrow$	$\downarrow \rightarrow \uparrow$
$\frac{\bar{u}_{\lambda'}(p'_1)}{\sqrt{p'_1+}}$	γ^+	$\frac{u_{\lambda}(p_1)}{\sqrt{p_1+}}$	2
$\frac{\bar{u}_{\lambda'}(p'_1)}{\sqrt{p'_1+}}$	γ^-	$\frac{2}{p'_1+ p_1^+} (\mathbf{p}'_{1\perp} \cdot \mathbf{p}_{1\perp} \pm i\mathbf{p}'_{1\perp} \times \mathbf{p}_{1\perp} + m_1^2)$	$\mp \frac{2m_1}{p'_1+ p_1^+} [(p'_1{}^{R(L)} - p_1{}^{R(L)})]$
$\frac{\bar{u}_{\lambda'}(p'_1)}{\sqrt{p'_1+}}$	γ_\perp^i	$\frac{\mathbf{p}'_{1\perp}^i \mp i\epsilon^{ij} \mathbf{p}'_{1\perp}^j}{p'_1+} + \frac{\mathbf{p}'_{1\perp}^i \pm i\epsilon^{ij} \mathbf{p}'_{1\perp}^j}{p_1^+}$	$\mp m_1 \left(\frac{p'_1+ - p_1^+}{p'_1+ p_1^+} \right) (\delta^{ix} \pm i\delta^{iy})$
$\frac{\bar{u}_{\lambda'}(p'_1)}{\sqrt{p'_1+}}$	$\mathbf{1}$	$\frac{m_1(p'_1+ + p_1^+)}{p'_1+ p_1^+}$	$\mp \frac{(p_1^+ p'_1{}^{R(L)} - p'_1+ p_1{}^{R(L)})}{p'_1+ p_1^+}$

TABLE II. Spin factors $S^{[\Gamma]}$ and Lorentz prefactors $\mathcal{P}_{\text{pBT}}^{[\Gamma]}$ and $\mathcal{P}_{\text{fBT}}^{[\Gamma]}$ for the vector ($\Gamma = \gamma^\mu$) and scalar ($\Gamma = \mathbf{1}$) currents, where $\mathcal{B} = (\mathcal{A}^2 + \mathbf{k}_\perp \cdot \mathbf{k}'_\perp)(\mathbf{k}_\perp^2 + \mathbf{k}_\perp \cdot \mathbf{q}_\perp + m_1^2) + (1-x)|\mathbf{k}_\perp \times \mathbf{q}_\perp|^2$, and $M_-^2 = \bar{P} \cdot q = M_0'^2 - M_0^2$.

$\Gamma = (\gamma^\mu, \mathbf{1})$	$S^{[\Gamma]}$	$\mathcal{P}_{\text{pBT}}^{[\Gamma]}$	$\mathcal{P}_{\text{fBT}}^{[\Gamma]}$
γ^+	$\frac{2(\mathcal{A}^2 + \mathbf{k}_\perp \cdot \mathbf{k}'_\perp)}{\sqrt{\mathcal{A}^2 + \mathbf{k}_\perp^2} \sqrt{\mathcal{A}^2 + \mathbf{k}'_\perp^2}}$	$2P^+$	$2P^+$
γ_\perp^j	$\frac{(\mathcal{A}^2 + \mathbf{k}_\perp \cdot \mathbf{k}'_\perp)(\mathbf{q}_\perp^j + 2\mathbf{k}_\perp^j)}{xP^+ \sqrt{\mathcal{A}^2 + \mathbf{k}_\perp^2} \sqrt{\mathcal{A}^2 + \mathbf{k}'_\perp^2}}$	\mathbf{q}_\perp^j	$\mathbf{q}_\perp^j \left(1 + \frac{M_-^2}{\mathbf{q}_\perp^2} \right)$
γ^-	$\frac{2\mathcal{A}m_1(1-x)\mathbf{q}_\perp^2 + 2\mathcal{B}}{(xP^+)^2 \sqrt{\mathcal{A}^2 + \mathbf{k}_\perp^2} \sqrt{\mathcal{A}^2 + \mathbf{k}'_\perp^2}}$	$\frac{2M^2 + \mathbf{q}_\perp^2}{P^+}$	$\frac{2M_0'^2 \mathbf{q}_\perp^2 + \mathbf{q}_\perp^4 + (M_-^2)^2}{\mathbf{q}_\perp^2 P^+}$
$\mathbf{1}$	$\frac{2m_1(\mathcal{A}^2 + \mathbf{k}_\perp \cdot \mathbf{k}'_\perp) + \mathcal{A}(1-x)\mathbf{q}_\perp^2}{xP^+ \sqrt{\mathcal{A}^2 + \mathbf{k}_\perp^2} \sqrt{\mathcal{A}^2 + \mathbf{k}'_\perp^2}}$	$2M$	$2M_0$

where the physical mass M in $\mathcal{P}_{\text{pBT}}^{[\gamma^-]}$ and $\mathcal{P}_{\text{pBT}}^{[\mathbf{1}]}$ is a constant and does not depend on the internal kinematics. In this case, the γ^+ and γ^\perp components reproduce the current-component independent fBT result, $F_{\text{pBT}}^{[\gamma^+, \gamma^\perp]} = F_{\text{fBT}}^{[\gamma^\mu]}$, whereas the γ^- component acquires a zero-mode contribution. Consequently, without an explicit zero-mode treatment, one obtains $F_{\text{pBT}}^{[\gamma^-]} \neq F_{\text{fBT}}^{[\gamma^-]}$.

Finally, Eqs. (28) and (29) give the quark-sector contribution to the EMFF obtained in fBT- and pBT-LFQMs, respectively, i.e. $F_{\text{fBT(pBT)}}^{[\gamma^\mu]}(Q^2, m_1, m_2)$ with $m_q = m_1$. The corresponding antiquark contribution ($m_{\bar{q}} = m_2$) is obtained by interchanging $m_q \leftrightarrow m_{\bar{q}}$ in Eq. (28), leading to the total EMFF:

$$F_{\text{em}}(Q^2) = e_q F_{\text{fBT(pBT)}}^{[\gamma^\mu]}(Q^2, m_q, m_{\bar{q}}) + e_{\bar{q}} F_{\text{fBT(pBT)}}^{[\gamma^\mu]}(Q^2, m_{\bar{q}}, m_q). \quad (30)$$

The pBT- and fBT-LFQM results for the matrix elements $\langle P | \bar{q}(0) \Gamma q(0) | P \rangle_{\text{BT}}$ and for the associated Lorentz prefactors $\mathcal{P}_{\text{pBT}}^{[\Gamma]}(0)$ and $\mathcal{P}_{\text{fBT}}^{[\Gamma]}(0)$ in the forward limit ($Q^2 \rightarrow 0$) are summarized in Table III. Two remarks are in order for the vector projections $\Gamma = \gamma^\perp$ and $\Gamma = \gamma^-$.

a. *Transverse component* $\Gamma = \gamma^\perp$. For the transverse current ($\gamma^\perp \equiv \{\gamma^1, \gamma^2\}; j = 1, 2$), the extraction of

TABLE III. Forward limit ($Q^2 \rightarrow 0$) matrix elements $\langle P | \bar{q}(0) \Gamma q(0) | P \rangle_{\text{BT}}$ and the corresponding Lorentz prefactors $\mathcal{P}_{\text{fBT}}^{[\Gamma]}(0)$ and $\mathcal{P}_{\text{pBT}}^{[\Gamma]}(0)$ in the fBT- and pBT-LFQMs. Note that $[d^3 \mathbf{k}] = \frac{P^+ dx d^2 \mathbf{k}_\perp}{(2\pi)^3}$.

Γ	$\langle P \bar{q}(0) \Gamma q(0) P \rangle_{\text{BT}}$	$\mathcal{P}_{\text{pBT}}^{[\Gamma]}(0)$	$\mathcal{P}_{\text{fBT}}^{[\Gamma]}(0)$
γ^+	$\int [d^3 \mathbf{k}] \phi(x, \mathbf{k}_\perp) ^2 \cdot 2$	$2P^+$	$2P^+$
γ_\perp^j	$\int [d^3 \mathbf{k}] \phi(x, \mathbf{k}_\perp) ^2 \cdot \left(\frac{2\mathbf{k}_\perp^j}{xP^+} \right)$	0	$\frac{2\mathbf{k}_\perp^j}{x}$
γ^-	$\int [d^3 \mathbf{k}] \phi(x, \mathbf{k}_\perp) ^2 \cdot \left(\frac{2(\mathbf{k}_\perp^2 + m_1^2)}{(xP^+)^2} \right)$	$\frac{2M^2}{P^+}$	$\frac{2(M_0'^2 + \frac{2k_x^2}{x^2})}{P^+}$
$\mathbf{1}$	$\int [d^3 \mathbf{k}] \phi(x, \mathbf{k}_\perp) ^2 \cdot \left(\frac{2m_1}{xP^+} \right)$	$2M$	$2M_0$

$F^{(\perp)}(0)$ from Table II and Eq. (26) requires a careful forward-limit procedure. In the strict $Q^2 \rightarrow 0$ limit, both the matrix element $\langle P | \bar{q} \gamma_\perp^j q | P \rangle_{\text{BT}}$ and the corresponding Lorentz prefactor $\mathcal{P}_{\text{pBT/fBT}}^{[\gamma_\perp^j]}(0)$ vanish. To obtain a finite result, we first contract the current γ_\perp^j with q_\perp^j and

then take the limit:

$$F_{\text{pBT}}^{[\gamma^\perp]}(Q^2) = \frac{\langle P | \bar{q}(0) (\gamma^\perp \cdot \mathbf{q}_\perp) q(0) | P \rangle_{\text{BT}}}{\mathcal{P}_{\text{pBT}}^{[\gamma^\perp]}(0) \cdot \mathbf{q}_\perp}, \quad (31)$$

$$F_{\text{fBT}}^{[\gamma^\perp]}(Q^2) = \left\langle P \left| \frac{\bar{q}(0) (\gamma^\perp \cdot \mathbf{q}_\perp) q(0)}{\mathcal{P}_{\text{fBT}}^{[\gamma^\perp]}(0) \cdot \mathbf{q}_\perp} \right| P \right\rangle_{\text{BT}}. \quad (32)$$

Numerically we find $F_{\text{pBT}}^{[\gamma^\perp]}(Q^2) = F_{\text{fBT}}^{[\gamma^\perp]}(Q^2)$ and $F_{\text{pBT}}^{[\gamma^\perp]}(0) = F_{\text{fBT}}^{[\gamma^\perp]}(0) = 1$, demonstrating that the transverse component is free of LF zero-mode contamination in both formulations.

In particular, at the integrand level in the forward limit, one finds for the fBT-LFQM

$$\lim_{Q^2 \rightarrow 0} S^{[\gamma^\perp \mathbf{q}_\perp]} = \lim_{Q^2 \rightarrow 0} \frac{2 \mathbf{k}_\perp \cdot \mathbf{q}_\perp}{x P^+}, \quad (33)$$

$$\lim_{Q^2 \rightarrow 0} (\mathcal{P}_{\text{fBT}}^{[\gamma^\perp]}(0) \cdot \mathbf{q}_\perp) = \lim_{Q^2 \rightarrow 0} \frac{2 \mathbf{k}_\perp \cdot \mathbf{q}_\perp}{x}, \quad (34)$$

whereas in the pBT-LFQM

$$\lim_{Q^2 \rightarrow 0} (\mathcal{P}_{\text{pBT}}^{[\gamma^\perp]}(0) \cdot \mathbf{q}_\perp) = \lim_{Q^2 \rightarrow 0} \mathbf{q}_\perp^2. \quad (35)$$

Consequently, in the fBT-LFQM the transverse-component normalization in the forward limit coincides with that obtained from the plus component,

$$\lim_{Q^2 \rightarrow 0} \left\langle P \left| \frac{\bar{q}(0) (\gamma^\perp \cdot \mathbf{q}_\perp) q(0)}{\mathcal{P}_{\text{fBT}}^{[\gamma^\perp]}(0) \cdot \mathbf{q}_\perp} \right| P \right\rangle_{\text{BT}} = \int [d^3 \mathbf{k}] |\phi(x, \mathbf{k}_\perp)|^2. \quad (36)$$

Accordingly, we present the forward-limit matrix element $\langle P | \bar{q}(0) \gamma_\perp^j q(0) | P \rangle_{\text{BT}}$ and the Lorentz prefactors $\mathcal{P}_{\text{pBT}}^{[\gamma_\perp^j]}(0)$ and $\mathcal{P}_{\text{fBT}}^{[\gamma_\perp^j]}(0)$ as effective forward-limit expressions inferred from the $\gamma^\perp \cdot \mathbf{q}_\perp$ analysis, namely by contracting both the numerator and the prefactor with \mathbf{q}_\perp and then taking the limit $Q^2 \rightarrow 0$ (see Table III).

b. *Minus component* $\Gamma = \gamma^-$. In the pBT-LFQM, the Lorentz prefactor in the forward limit reduces to

$$\mathcal{P}_{\text{pBT}}^{[\gamma^-]}(0) = \frac{2M^2}{P^+}. \quad (37)$$

In the fBT-LFQM, the covariant prefactor is implemented pointwise under the (x, \mathbf{k}_\perp) integral with the BT replacement $M \rightarrow M_0$. For the minus component this yields, at the integrand level,

$$\mathcal{P}_{\text{fBT}}^{[\gamma^-]}(0) = \frac{2}{P^+} \left(M_0^2 + \frac{2k_x^2}{x^2} \right) \equiv \frac{2\mathcal{M}_{\text{BT}}^2}{P^+}, \quad (38)$$

where we define

$$\mathcal{M}_{\text{BT}}^2 \equiv M_0^2 + \frac{2k_x^2}{x^2}. \quad (39)$$

The k_x dependence originates from the $M_0^2 = M_0'^2 - M_0^2$ term, and $\mathbf{k}_\perp \cdot \mathbf{q}_\perp = |\mathbf{k}_\perp| |\mathbf{q}_\perp| \cos \theta \equiv k_x |\mathbf{q}_\perp|$. Although

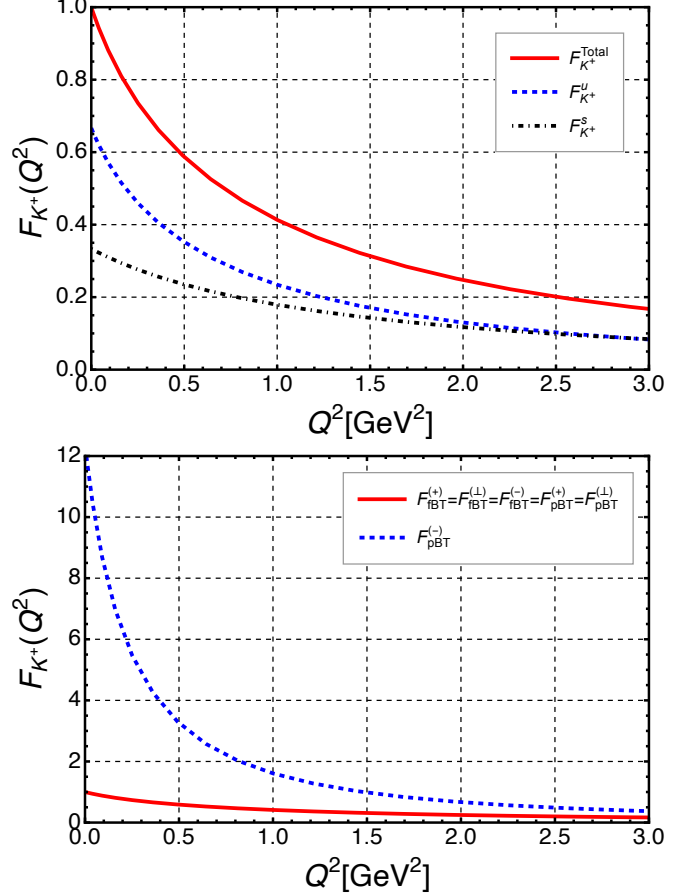


FIG. 1. Charged-kaon EMFF $F_{K+}(Q^2)$. Top: fBT-LFQM total (solid) with u (dashed) and s (dotted) contributions. Bottom: exact, component-independent benchmark (solid) vs. pBT-LFQM γ^- extraction (dashed), showing the missing LF zero mode.

$\mathcal{P}_{\text{fBT}}^{[\gamma^-]}$ retains this angular dependence locally, the extracted form factor remains component-independent:

$$F_{\text{fBT}}^{[\gamma^-]}(0) = \lim_{Q^2 \rightarrow 0} \left\langle P \left| \frac{\bar{q}(0) \gamma^- q(0)}{\mathcal{P}_{\text{fBT}}^{[\gamma^-]}(0)} \right| P \right\rangle_{\text{BT}} = 1. \quad (40)$$

By contrast, in the pBT-LFQM the use of the physical mass M in the Lorentz prefactor, together with the omission of the LF zero-mode contribution, generally spoils the normalization,

$$F_{\text{pBT}}^{[\gamma^-]}(0) = \lim_{Q^2 \rightarrow 0} \frac{\langle P | \bar{q}(0) \gamma^- q(0) | P \rangle_{\text{BT}}}{\mathcal{P}_{\text{pBT}}^{[\gamma^-]}(0)} \neq 1. \quad (41)$$

Restoration of the correct charge normalization requires the inclusion of the LF zero-mode contribution in the pBT-LFQM. This underscores that the fBT-LFQM effectively accounts for the physics that would otherwise manifest as the LF zero modes, which are absent in the formulation.

In the top panel of Fig. 1, we show our fBT-LFQM prediction for the charged-kaon EMFF $F_{K+}(Q^2)$. The solid

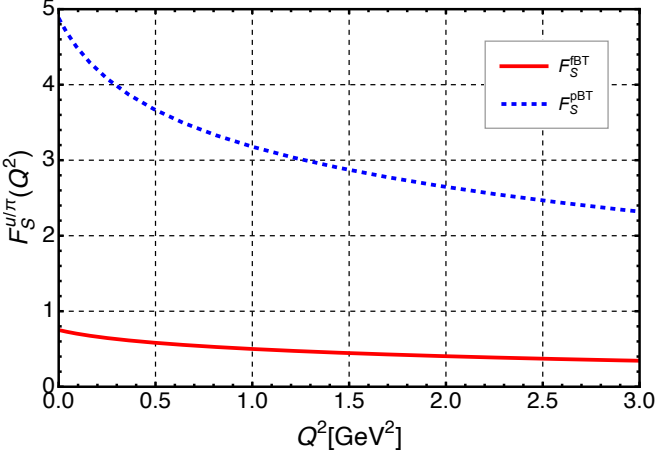


FIG. 2. The u -quark contribution to the mass-factored scalar form factor $F_S^{u/\pi}(Q^2)$ of the π^+ obtained in the fBT-LFQM (solid) and pBT-LFQM (dashed).

curve shows the total result, while the dashed and dotted curves show the separate u - and s -quark contributions, respectively. The extraction is independent of the current component ($\mu = +, \perp, -$) and satisfies charge normalization at $Q^2 = 0$. As shown in the bottom panel of Fig. 1, the pBT-LFQM results extracted from the γ^+ and γ^\perp components coincide with the exact, current-component-independent benchmark (solid), whereas the result extracted from the γ^- component (dashed) shows a significant deviation. This deviation from the solid curve quantifies the missing LF zero-mode contribution to the minus component of the current in the pBT-LFQM formulation.

In Fig. 2 we show the u -quark contribution to the mass-factored scalar form factor $F_S^{u/\pi}(Q^2)$ of the π^+ , obtained in the fBT-LFQM (solid) and pBT-LFQM (dashed). In the pBT-LFQM, the mass-factored form factor satisfies the identity $f_S(Q^2) = 2M_\pi F_S^{\text{pBT}}(Q^2)$ with the physical pion mass M_π . The direct scalar form factor $f_S(Q^2)$ itself is identical in both the fBT- and pBT-LFQMs, since it is obtained from the same underlying matrix element. By contrast, in the fBT-LFQM the consistent replacement $M_\pi \rightarrow M_0(x, \mathbf{k}_\perp)$ inside the integrand implies $F_S^{\text{fBT}}(Q^2) \neq f_S(Q^2)/(2M_\pi)$. Numerically, our fBT-LFQM result gives $F_S^{\text{fBT}}(0) < 1$, while the pBT-LFQM extraction yields a value well above unity. This qualitative pattern mirrors the behavior seen for the EMFF extracted from the $(-)$ component in the pBT-LFQM, where sensitivity to LF zero modes leads to a systematic overestimate over the full Q^2 range, although its quantitative impact diminishes as Q^2 increases.

In Fig. 3 we show the u -quark (top) and s -quark (bottom) contributions to the mass-factored scalar form factor $F_S^{q/K}(Q^2)$ of the K^+ , obtained in the fBT-LFQM (solid) and pBT-LFQM (dashed). As seen in the figure, the s -quark contribution is larger than the u -quark contribution, reflecting SU(3) flavor breaking. As

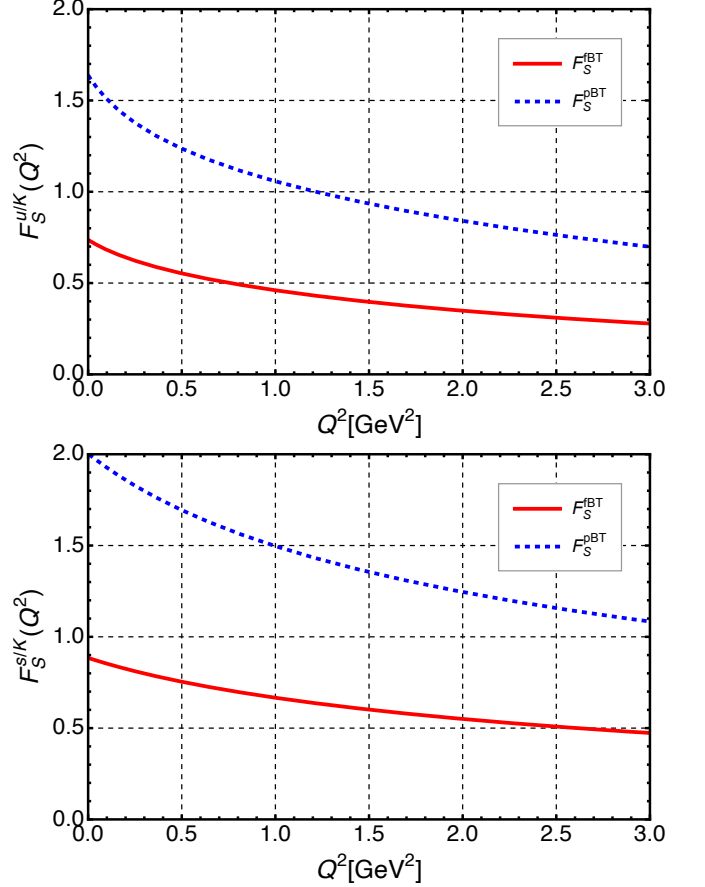


FIG. 3. The u -quark (top) and s -quark (bottom) contributions to the mass-factored scalar form factor $F_S^{q/K}(Q^2)$ of the K^+ , obtained in the fBT-LFQM (solid) and pBT-LFQM (dashed).

in the pion case, our fBT-LFQM result for the K^+ gives $F_S^{\text{fBT}}(0) < 1$, while the pBT-LFQM extraction $F_S^{\text{pBT}}(0) = f_S(0)/(2M_K)$ with the physical kaon mass M_K yields a value well above unity for both quark flavors, $q = u, s$.

IV. TMDS AND PDFS

A. Formal definitions of TMDs and PDFs

For the pseudoscalar meson state $|P\rangle$ defined in Eq. (4), the valence-quark TMDs are defined via the quark-quark correlator [27–30, 32] ¹

$$\Phi_q^{[\Gamma]}(x, \mathbf{k}_\perp) = \frac{1}{2} \int [d^3 z] e^{ik \cdot z} \langle P | \bar{q}(0) \Gamma q(z) | P \rangle |_{z^+ = 0}, \quad (42)$$

¹ In constituent-quark models without explicit gluon degrees of freedom, the Wilson line $\mathcal{W}(0, z)$ in the QCD definition reduces to the identity in color space.

where $[d^3z] \equiv \frac{dz^- d^2\mathbf{z}_\perp}{2(2\pi)^3}$, and the momentum variables are defined by $k^+ = xP^+$ and \mathbf{k}_\perp in a frame where $\mathbf{P}_\perp = 0$. Here $q(z)$ is the quark field operator and Γ specifies the Dirac projection of the correlator $\Phi_q^{[\Gamma]}(x, \mathbf{k}_\perp)$, with the subscript q denoting flavor. Integrating both sides of Eq. (42) over x and \mathbf{k}_\perp yields the forward matrix element

$$\int dx \int d^2\mathbf{k}_\perp \Phi_q^{[\Gamma]}(x, \mathbf{k}_\perp) = \frac{1}{2P^+} \langle P | \bar{q}(0) \Gamma q(0) | P \rangle \quad (43)$$

and the derivation is given in Appendix A.

In the pBT-LFQM, the unpolarized T -even TMDs are defined by the projections [27, 28]²

$$\Phi_q^{[\gamma^+]}(x, \mathbf{k}_\perp) = f_1^q(x, \mathbf{k}_\perp), \quad (44a)$$

$$\Phi_q^{[\gamma_\perp^j]}(x, \mathbf{k}_\perp) = \frac{\mathbf{k}_\perp^j}{P^+} f^{\perp q}(x, \mathbf{k}_\perp), \quad (j = 1, 2) \quad (44b)$$

$$\Phi_q^{[\gamma^-]}(x, \mathbf{k}_\perp) = \frac{M^2}{(P^+)^2} f_4^q(x, \mathbf{k}_\perp), \quad (44c)$$

$$\Phi_q^{[1]}(x, \mathbf{k}_\perp) = \frac{M}{P^+} e^q(x, \mathbf{k}_\perp). \quad (44d)$$

Here, f_1^q , $f^{\perp q}$, and f_4^q originate from vector projections, while e^q is associated with the scalar projection.

Integrating a generic TMD over transverse momentum yields the corresponding (collinear) PDF,

$$f(x) = \int d^2\mathbf{k}_\perp f(x, \mathbf{k}_\perp). \quad (45)$$

Unlike f_1^q , e^q , and f_4^q , the $f^{\perp q}$ projection is proportional to \mathbf{k}_\perp^j and $\int d^2\mathbf{k}_\perp \mathbf{k}_\perp^j f(x, \mathbf{k}_\perp) = 0$ by azimuthal symmetry. Nevertheless, we define the formal collinear integral $f^{\perp q}(x) \equiv \int d^2\mathbf{k}_\perp f^{\perp q}(x, \mathbf{k}_\perp)$, following Refs. [27, 28].

In both the pBT- and fBT-LFQMs, the $\Gamma = \gamma^+$ and $\Gamma = \gamma_\perp^j$ projections (Eqs. (44a)–(44b)) are free of LF zero modes, so that f_1^q and $f^{\perp q}$ are determined entirely by the on-shell (valence) correlator.

In our conventions,³

$$\begin{aligned} f_1^q(x, \mathbf{k}_\perp) &= \frac{|\phi(x, \mathbf{k}_\perp)|^2}{2(2\pi)^3}, \\ f^{\perp q}(x, \mathbf{k}_\perp) &= \frac{1}{x} f_1^q(x, \mathbf{k}_\perp). \end{aligned} \quad (46)$$

The twist-2 PDF $f_1^q(x)$ satisfies the number and momentum sum rules,

$$\begin{aligned} \int_0^1 dx f_1^q(x) &= N_q, \\ \sum_q \int_0^1 dx x f_1^q(x) &= 1, \end{aligned} \quad (47)$$

² For a spin-0 target these correspond, respectively, to twist-2 (f_1), twist-3 ($f^{\perp q}$ and e), and twist-4 (f_4) unpolarized structures.

³ The overall sign of $f^{\perp q}(x, \mathbf{k}_\perp)$ depends on the definition of $\mathbf{k}_{1\perp} = \pm \mathbf{k}_\perp$, leading to $f^{\perp q}(x, \mathbf{k}_\perp) = \pm \frac{1}{x} f_1^q(x, \mathbf{k}_\perp)$.

where N_q denotes the valence count of flavor q , e.g., $N_u = N_{\bar{s}} = 1$ for $K^+(u\bar{s})$.

B. Extraction of TMDs from $\Gamma = \{\gamma^-, \mathbf{1}\}$

The definitions in Eq. (44) must be consistent with EM charge normalization in the forward limit ($Q^2 = 0$), i.e., $F_{\text{pBT}}^{[\gamma^\mu]}(0) = F_{\text{fBT}}^{[\gamma^\mu]}(0) = 1$ (see Eqs. (20) and (22)).

In the pBT-LFQM, enforcing the γ^- component of Eq. (43) gives

$$\int dx \int d^2\mathbf{k}_\perp \frac{2P^+}{\mathcal{P}_{\text{pBT}}^{[\gamma^-]}(0)} \Phi_q^{[\gamma^-]}(x, \mathbf{k}_\perp) = F_{\text{pBT}}^{[\gamma^-]}(0) = 1, \quad (48)$$

with $\mathcal{P}_{\text{pBT}}^{[\gamma^-]}(0) = 2P^- = 2M^2/P^+$ the kinematic projector for the γ^- current in the pBT-LFQM realization. Using Eq. (44c) one then obtains

$$\int dx \int d^2\mathbf{k}_\perp f_4^q(x, \mathbf{k}_\perp) = F_{\text{pBT}}^{[\gamma^-]}(0) = 1, \quad (49)$$

and the explicit expression

$$f_4^q(x, \mathbf{k}_\perp) = \frac{(P^+)^2}{M^2} \Phi_q^{[\gamma^-]}(x, \mathbf{k}_\perp) = \frac{\mathbf{k}_\perp^2 + m_1^2}{x^2 M^2} f_1^q(x, \mathbf{k}_\perp), \quad (50)$$

where m_1 is the struck-quark mass. However, if LF zero modes are not properly identified and included, one generally finds $F_{\text{pBT}}^{[\gamma^-]}(0) \neq 1$, so the sum rule

$$\int_0^1 dx f_4^q(x) \equiv \int dx \int d^2\mathbf{k}_\perp f_4^q(x, \mathbf{k}_\perp) = N_q \quad (51)$$

is generally violated.

In the fBT-LFQM, Eq. (43) becomes

$$\int dx \int d^2\mathbf{k}_\perp \frac{2P^+}{\mathcal{P}_{\text{fBT}}^{[\gamma^-]}(0)} \Phi_q^{[\gamma^-]}(x, \mathbf{k}_\perp) = F_{\text{fBT}}^{[\gamma^-]}(0) = 1, \quad (52)$$

with $\mathcal{P}_{\text{fBT}}^{[\gamma^-]}(0) = 2\mathcal{M}_{\text{BT}}^2/P^+$. Defining

$$f_4^q(x, \mathbf{k}_\perp) = \frac{(P^+)^2}{\mathcal{M}_{\text{BT}}^2} \Phi_q^{[\gamma^-]}(x, \mathbf{k}_\perp) = \frac{\mathbf{k}_\perp^2 + m_1^2}{x^2 \mathcal{M}_{\text{BT}}^2} f_1^q(x, \mathbf{k}_\perp), \quad (53)$$

the sum rule in Eq. (51) is now satisfied and the extraction is component-independent. We note a factor-of-two difference with Refs. [27, 28] arising from light-front conventions. Our normalization leads to Eq. (51), whereas Refs. [27, 28] obtain $2 \int_0^1 dx f_4^q(x) = N_q$.⁴

⁴ The origin is the choice of LF $+/$ components: we use a convention in which, at $\mathbf{P}_\perp = 0$, $M^2 = P^+ P^-$, while Refs. [27, 28] adopt the alternative normalization yielding $M^2 = 2P^+ P^-$. Equivalently, this is the difference between defining $a^\pm = a^0 \pm a^3$ vs. $a^\pm = (a^0 \pm a^3)/\sqrt{2}$.

Positivity inequalities also provide an important test for the validation of the TMDs [27, 28] which require $f_1^q(x, \mathbf{k}_\perp) \geq 0$ and $f_4^q(x, \mathbf{k}_\perp) \geq 0$. In contrast, the positivity of $f^{\perp q}(x, \mathbf{k}_\perp)$ depends on the transverse momentum assignment: choosing $\mathbf{k}_{1\perp} = \mathbf{k}_\perp$ leads to a positive constraint, while $\mathbf{k}_{1\perp} = -\mathbf{k}_\perp$ results in a negative one.

For the scalar current case, since the forward limit matrix element satisfies $\langle P|\bar{q}(0)\mathbf{1}q(0)|P\rangle_{\text{BT}} = 2MF_S^q(0)$, Eq. (43) becomes for $\Gamma = \mathbf{1}$,

$$\begin{aligned} \int dx \int d^2\mathbf{k}_\perp \Phi_q^{[1]}(x, \mathbf{k}_\perp) &= \frac{1}{2P^+} \langle P|\bar{q}(0)\mathbf{1}q(0)|P\rangle_{\text{BT}} \\ &= \frac{M}{P^+} F_S^q(0). \end{aligned} \quad (54)$$

From this relation, together with the result of $\langle P|\bar{q}(0)\mathbf{1}q(0)|P\rangle_{\text{BT}}$ given in Table II, one obtains

$$\Phi_q^{[1]}(x, \mathbf{k}_\perp) = \frac{M}{P^+} e^q(x, \mathbf{k}_\perp) = f_1^q(x, \mathbf{k}_\perp) \frac{m_1}{xP^+}. \quad (55)$$

Thus in the pBT-LFQM, e^q is obtained as [27, 28]

$$e^q(x, \mathbf{k}_\perp) = \frac{m_1}{xM} f_1^q(x, \mathbf{k}_\perp), \quad (56)$$

while in the fBT-LFQM, we obtain

$$e^q(x, \mathbf{k}_\perp) = \frac{m_1}{xM_0} f_1^q(x, \mathbf{k}_\perp). \quad (57)$$

C. Internal consistency of the LFQM

Testing the internal consistency of the LFQM is essential, since the model describes free on-shell quarks and does not explicitly include gluonic Fock states. In this work, we contrast the pBT-LFQM with the fBT-LFQM.

As shown in the previous subsections, the pBT-LFQM [27, 28] satisfies

$$\begin{aligned} x e^q(x, \mathbf{k}_\perp) &= \frac{m_q}{M} f_1^q(x, \mathbf{k}_\perp), \\ x f^{\perp q}(x, \mathbf{k}_\perp) &= f_1^q(x, \mathbf{k}_\perp), \\ x^2 f_4^q(x, \mathbf{k}_\perp) &= \frac{\mathbf{k}_\perp^2 + m_q^2}{M^2} f_1^q(x, \mathbf{k}_\perp). \end{aligned} \quad (58)$$

However, the equalities involving e^q and f_4^q generally do not hold numerically in the pBT-LFQM unless LF zero-mode contributions are properly included. These zero modes arise in physical observables when the physical meson mass is used in conjunction with so-called “bad” current projections, particularly for $\Gamma = \gamma^-$ and $\Gamma = \mathbf{1}$.

Consistent with this, our recent analysis of the ρ -meson decay constants and beyond-leading-twist DAs [91] showed that the QCD equation of motion (EOM) relation $f_\rho^S = f_\rho^\perp - \frac{2m}{M} f_\rho^\parallel$ between the scalar (f_ρ^S), vector/longitudinal (f_ρ^\parallel), and tensor/transverse (f_ρ^\perp) decay constants fails in the pBT-LFQM but is restored in the

fBT-LFQM. We therefore employ the fBT-LFQM formulation whenever component independence and EOM consistency are critical (notably for the γ^- and scalar projections).

In the fBT-LFQM, analogous consistency relations hold with the following replacements:

$$\begin{aligned} x e^q(x, \mathbf{k}_\perp) &= \frac{m_q}{M_0} f_1^q(x, \mathbf{k}_\perp), \\ x f^{\perp q}(x, \mathbf{k}_\perp) &= f_1^q(x, \mathbf{k}_\perp), \\ x^2 f_4^q(x, \mathbf{k}_\perp) &= \frac{\mathbf{k}_\perp^2 + m_q^2}{M_{\text{BT}}^2} f_1^q(x, \mathbf{k}_\perp). \end{aligned} \quad (59)$$

These relations illustrate that the fBT-LFQM preserves the EOM structure of QCD while ensuring covariance through the use of the invariant mass $M_0(M_0')$ instead of the physical mass $M(M')$ in Lorentz prefactors.

In Fig. 4 we compare the u -quark PDFs: $f_4^{u/K}(x)$ and $e^{u/K}(x)$, obtained from our fBT-LFQM (solid) and from the pBT-LFQM (dashed). As discussed above, the fBT-LFQM result satisfies the $f_4^{u/K}$ sum rule of Eq. (51), whereas the pBT-LFQM result does not. This difference quantifies the LF zero-mode contribution to $f_4^{u/K}(x)$ that is missed in the pBT-LFQM scheme. For $e^{u/K}(x)$ we observe a similar difference. Because the scalar channel has no conserved charge, its normalization is sensitive to the mass used in the Lorentz prefactor (M vs. M_0). In the pBT-LFQM the deviation may include LF zero-mode effects, although a dedicated analysis would be required to establish this unambiguously. By contrast, the fBT-LFQM extraction implements the replacement $M \rightarrow M_0$ consistently under the (x, \mathbf{k}_\perp) integral and is therefore self-consistent with the mass-factored definition in Eq. (19).

In the following numerical section, we present our fBT-LFQM results for the TMDs and PDFs.

V. NUMERICAL RESULT

A. TMDs and Transverse Moments

Figure 5 shows contour maps of the unpolarized T-even TMDs $f(x, \mathbf{k}_\perp)$ with $f \in \{f_1^q, f^{\perp q}, e^q, f_4^q\}$ for the u quark in π^+ (top) and K^+ (middle), and for the s quark in K^+ (bottom), plotted in the (x, \mathbf{k}_\perp) plane (color scale: red = high, violet = low). While f_1^q , $f^{\perp q}$, and e^q are azimuthally symmetric, the twist-4 TMD f_4^q is not. The BT prefactor M_{BT}^2 given by Eq. (39) breaks O(2) symmetry at the integrand level and induces an elliptic (k_x, k_y) dependence. For the (x, \mathbf{k}_\perp) panels we therefore fix $\theta = \pi/2$ (so $k_x = 0$), which minimizes the denominator (by setting $k_x = 0$) and thus maximizes f_4^q , enabling transparent cross-panel comparisons.

For the twist-2 pion TMD, $f_1^{u/\pi}$, the (x, \mathbf{k}_\perp) contour is symmetric under $x \leftrightarrow 1-x$ and shows two highest-density (red) lobes at small k_\perp near the endpoints of x . As

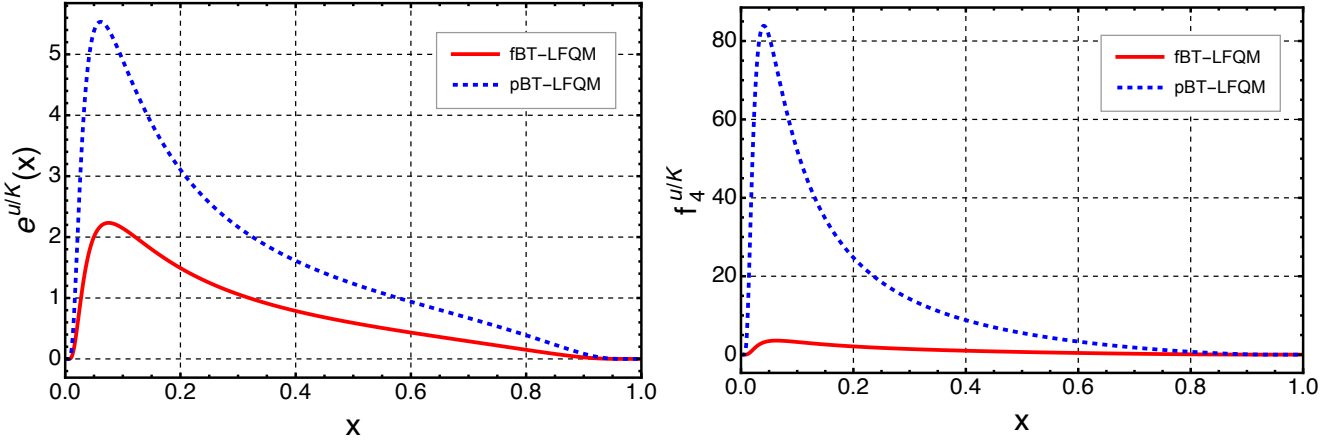


FIG. 4. Comparison of u -quark PDFs in K^+ : $e^{u/K}(x)$ (left) and $f_4^{u/K}(x)$ (right), shown for the fBT-LFQM (solid) and the pBT-LFQM (dashed).

k_\perp increases, the density diminishes symmetrically about $x = \frac{1}{2}$, reflecting SU(2) isospin symmetry with $m_u = m_d$. This double-hump pattern at low k_\perp does not contradict the PDF, since integration over transverse momentum yields a single peak near $x = \frac{1}{2}$. In the kaon, SU(3) flavor breaking shifts the distributions, with $f_1^{u/K}$ moving toward smaller x and $f_1^{s/K}$ toward larger x , resulting in single-lobe contours.

In contrast, the higher-twist TMDs $f^{\perp q}$, e^q , and f_4^q are sensitive to the quark flavor through factors such as (m_q/M_0) and $(\mathbf{k}_\perp^2 + m_q^2)/\mathcal{M}_{\text{BT}}^2$, which break simple Gaussian factorization and introduce ellipticity in f_4^q . As shown in Fig. 5, the u -quark distributions in both π^+ and K^+ form single-lobe patterns concentrated at small x and k_\perp . The s -quark higher-twist TMDs, $f^{\perp s/K}$ and $e^{s/K}$, have broader support in the (x, \mathbf{k}_\perp) plane than their u -quark counterparts and can display a mildly asymmetric two-lobe shape with a strong low- (x, \mathbf{k}_\perp) region and a weaker shoulder toward larger x . The twist-4 distribution $f_4^{s/K}$ is also broader and exhibits an elliptic angular dependence from the BT prefactor, decreasing gradually as both x and k_\perp increase.

For a generic TMD $f(x, \mathbf{k}_\perp)$, the n th transverse moment ($n \geq 1$) is defined as

$$\langle k_\perp^n \rangle = \frac{\int_0^1 dx \int d^2 \mathbf{k}_\perp k_\perp^n f(x, \mathbf{k}_\perp)}{\int_0^1 dx \int d^2 \mathbf{k}_\perp f(x, \mathbf{k}_\perp)}. \quad (60)$$

If the k_\perp dependence is isotropic and Gaussian in the transverse plane, $f(x, \mathbf{k}_\perp) \propto \exp[-\mathbf{k}_\perp^2/(2\sigma^2)]$, one obtains $\langle k_\perp \rangle = \sigma\sqrt{\pi/2}$ and $\langle k_\perp^2 \rangle = 2\sigma^2$, implying

$$R_G \equiv \frac{2}{\sqrt{\pi}} \frac{\langle k_\perp \rangle}{\langle k_\perp^2 \rangle^{1/2}} = 1. \quad (61)$$

We use R_G as a simple indicator of how closely the transverse-momentum distribution follows a Gaussian shape:

$R_G = 1$ for an exact Gaussian profile, while deviations from unity quantify non-Gaussian behavior. This diagnostic provides a means to assess the accuracy of the Gaussian Ansatz often adopted to describe the transverse-momentum dependence in DIS and related analyses [92–94].

In our fBT-LFQM, the Gaussian LFWF $\phi(x, \mathbf{k}_\perp)$ is given by Eq. (13), and the twist-2 TMD is expressed as $f_1^q(x, \mathbf{k}_\perp) \propto |\phi(x, \mathbf{k}_\perp)|^2$. Using the variable transformation $(\partial k_z / \partial x) dx = dk_z$, the x integration converts into an integral over k_z , so that any x -integrated quantity becomes a three-dimensional (3D) isotropic Gaussian in (k_x, k_y, k_z) . In particular, the x -integrated transverse-momentum profile $f_1^q(\mathbf{k}_\perp) \equiv \int_0^1 dx f_1^q(x, \mathbf{k}_\perp)$ is a purely 2D Gaussian,

$$\int_{-\infty}^{\infty} dk_z e^{-(k_z^2 + k_z^2)/\beta^2} \propto e^{-\mathbf{k}_\perp^2/\beta^2}, \quad (62)$$

so that $f_1^q(\mathbf{k}_\perp) \propto \exp(-\mathbf{k}_\perp^2/\beta^2)$. Comparing with the generic form $\exp(-\mathbf{k}_\perp^2/2\sigma^2)$ gives $\sigma = \beta/\sqrt{2}$, hence

$$\langle k_\perp^2 \rangle = \beta^2, \quad \langle k_\perp \rangle = \frac{\beta}{2}\sqrt{\pi},$$

and consequently $R_G = 1$ holds exactly for this ansatz. Thus, in the fBT-LFQM, the intrinsic root-mean-square (RMS) transverse width $\langle k_\perp^2 \rangle^{1/2}$ that governs the k_\perp structure is directly determined by the variational parameter β .

The exact Gaussian result for $f_1^q(\mathbf{k}_\perp)$, and hence $R_G = 1$, relies on the Jacobian factor $\sqrt{\partial k_z / \partial x}$ in $\phi(x, \mathbf{k}_\perp)$. With this factor included, the x -integration becomes an integral over k_z and yields $f_1^q(\mathbf{k}_\perp) \propto e^{-\mathbf{k}_\perp^2/\beta^2}$. If the Jacobian factor is omitted, an additional weight $(\partial x / \partial k_z)$ remains inside the k_z integral, yielding a k_\perp -dependent prefactor. The transverse profile then ceases to be purely Gaussian, and in general $R_G \neq 1$.

In Table IV we summarize our predictions for $\langle k_\perp \rangle$, $\langle k_\perp^2 \rangle^{1/2}$, and the dimensionless ratio R_G for the u -quark

TABLE IV. Values of $\langle k_{\perp} \rangle$ and $\langle k_{\perp}^2 \rangle^{1/2}$ (in GeV), and the ratio R_G , for the u -quark TMD in the π^+ and K^+ .

Model	Hadron	Quantity	f_1^u	e^u	$f^{\perp u}$	f_4^u
This Work	$\pi^+(u\bar{d})$	$\langle k_{\perp} \rangle$	0.3243	0.2608	0.2912	0.2686
		$\langle k_{\perp}^2 \rangle^{1/2}$	0.3659	0.3014	0.3347	0.3172
	$K^+(u\bar{s})$	R_G	1.00	0.9763	0.9820	0.9556
		$\langle k_{\perp} \rangle$	0.3444	0.2735	0.2987	0.2840
	$K^+(u\bar{s})$	$\langle k_{\perp}^2 \rangle^{1/2}$	0.3886	0.3168	0.3450	0.3360
		R_G	1.00	0.9740	0.9770	0.9537
LCQM [29]	$\pi^+(u\bar{d})$	$\langle k_{\perp} \rangle$	0.22	0.18	0.21	0.21
		$\langle k_{\perp}^2 \rangle^{1/2}$	0.26	0.22	0.25	0.24
	$K^+(u\bar{s})$	R_G	0.96	0.95	0.96	0.95
		$\langle k_{\perp} \rangle$	0.26	0.21	0.23	0.23
	$K^+(u\bar{s})$	$\langle k_{\perp}^2 \rangle^{1/2}$	0.30	0.25	0.27	0.27
		R_G	0.98	0.96	0.96	0.96
LFHM [29]	$\pi^+(u\bar{d})$	$\langle k_{\perp} \rangle$	0.24	0.21	0.23	0.22
		$\langle k_{\perp}^2 \rangle^{1/2}$	0.27	0.24	0.26	0.25
	$K^+(u\bar{s})$	R_G	1.00	0.99	0.99	0.99
		$\langle k_{\perp} \rangle$	0.24	0.21	0.22	0.22
	$K^+(u\bar{s})$	$\langle k_{\perp}^2 \rangle^{1/2}$	0.27	0.24	0.25	0.25
		R_G	1.00	0.99	0.99	0.99
LFCM [28]	$\pi^+(u\bar{d})$	$\langle k_{\perp} \rangle$	0.28	0.26	0.26	0.30
		$\langle k_{\perp}^2 \rangle^{1/2}$	0.32	0.30	0.30	0.33
		R_G	0.99	0.99	0.99	0.98
BLFQ [30]	$\pi^+(u\bar{d})$	$\langle k_{\perp} \rangle$	0.26	0.26	0.25	-
		$\langle k_{\perp}^2 \rangle^{1/2}$	0.30	0.30	0.29	-
		R_G	0.98	0.98	0.97	-

TABLE V. Values of $\langle k_{\perp} \rangle$ and $\langle k_{\perp}^2 \rangle^{1/2}$ (in GeV), and the ratio R_G , for the s -quark TMD in the K^+ .

Model	Hadron	Quantity	f_1^s	e^s	$f^{\perp s}$	f_4^s
This Work	$K^+(u\bar{s})$	$\langle k_{\perp} \rangle$	0.3444	0.3100	0.3402	0.3032
		$\langle k_{\perp}^2 \rangle^{1/2}$	0.3886	0.3523	0.3843	0.3498
		R_G	1.00	0.9930	0.9989	0.9781
LCQM [29]	$K^+(u\bar{s})$	$\langle k_{\perp} \rangle$	0.26	0.21	0.23	0.18
		$\langle k_{\perp}^2 \rangle^{1/2}$	0.30	0.25	0.27	0.21
		R_G	0.98	0.96	0.96	0.97
LFHM [29]	$K^+(u\bar{s})$	$\langle k_{\perp} \rangle$	0.23	0.20	0.21	0.19
		$\langle k_{\perp}^2 \rangle^{1/2}$	0.26	0.23	0.24	0.22
		R_G	1	0.98	0.99	0.97

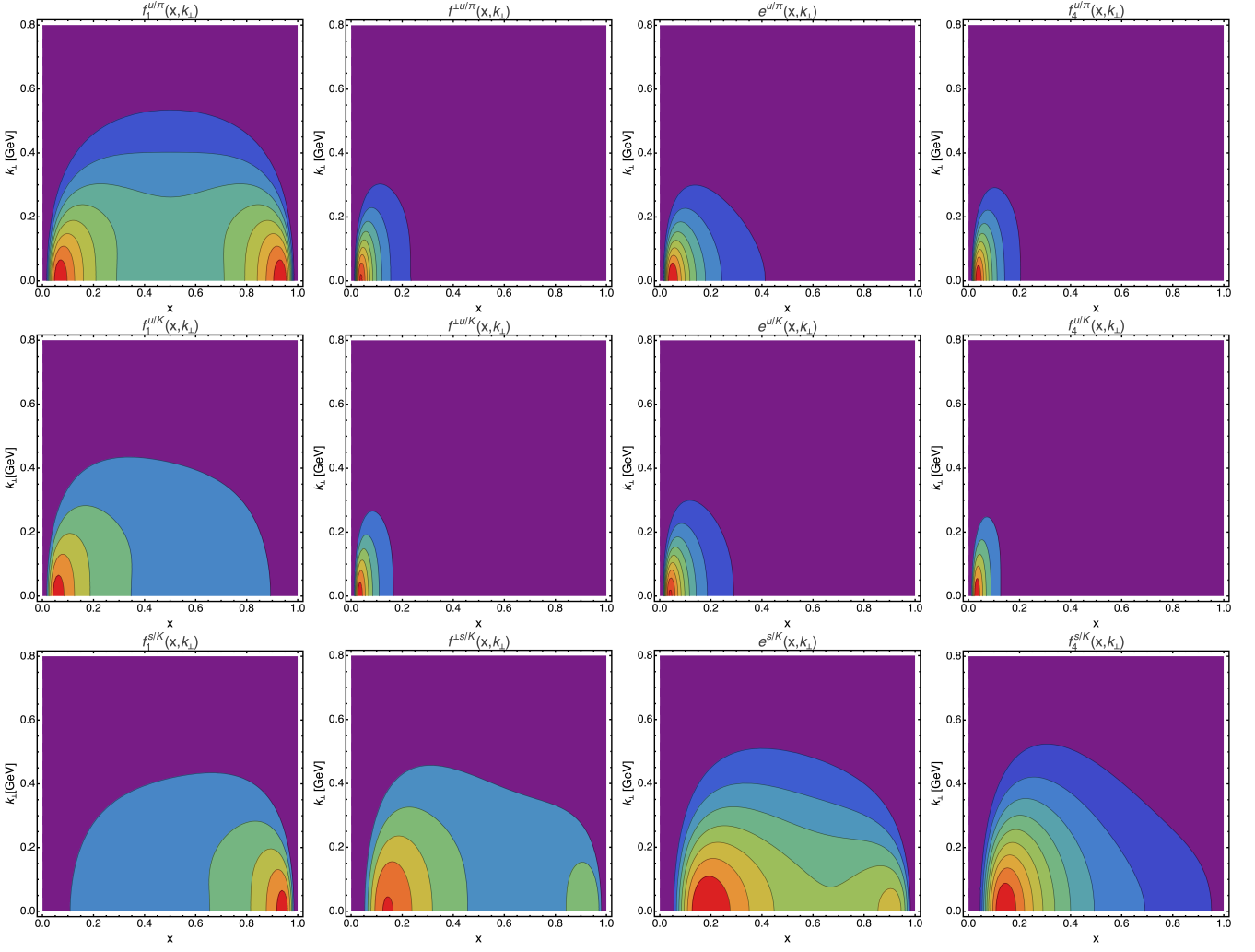


FIG. 5. Contour maps of the unpolarized T-even TMDs (f_1^q , $f_1^{\perp q}$, e^q , f_4^q) for u in π^+ (top), u in K^+ (middle), and s in K^+ (bottom), shown in the (x, k_\perp) plane (color: red = high, violet = low). For f_4^q we fix $\theta = \pi/2$ ($k_x = 0$) to display the maximal profile.

TMDs in π^+ and K^+ , together with other light-front model results from Refs. [28–30]. Table V reports the corresponding quantities for the s -quark TMDs in K^+ , compared with Ref. [29].

The mean and RMS transverse moments, $\langle k_\perp \rangle$ and $\langle k_\perp^2 \rangle^{1/2}$, exhibit a clear twist-ordered hierarchy across the unpolarized T-even TMDs: $f_1^q > f_1^{\perp q} > e^q > f_4^q$. This reflects not only twist counting (twist-2 > twist-3 > twist-4) but also additional chiral and kinematic suppressions within the same twist sector. Although $f_1^{\perp q}$ and e^q are both twist-3, their magnitudes differ due to the distinct projectors and kinematic prefactors entering their definitions. Eq. (59) shows that, pointwise in x and k_\perp , one finds $\frac{e^q}{f_1^{\perp q}} \simeq \frac{m_q}{M_0} < 1$, which explains why $f_1^{\perp q}$ is larger than e^q within the twist-3 sector.

Beyond twist ordering, two SU(3)-breaking trends are robust. First, across mesons the kaon moments exceed the pion's for a fixed flavor (e.g., u in K^+ vs. u in π^+). Second, within a given K^+ the s -quark moments ex-

ceed the u -quark's. The first trend is largely driven by a larger variational scale in the kaon, $\beta_{q\bar{s}} > \beta_{q\bar{q}}$. This implies a tighter coordinate-space wave function and, by Fourier conjugacy, broader momentum-space profiles. The second trend arises even at fixed $\beta_{q\bar{s}}$ from mass-asymmetric LF kinematics, skewed x distributions, larger typical $M_0(x, \mathbf{k}_\perp)$, and the Jacobian $\partial k_z / \partial x$, together with flavor-dependent projector factors. Finally, the twist-4 distribution f_4^q (see Eq. (59)) includes an additional anisotropic suppression through the explicit k_x dependence in $\mathcal{M}_{\text{BT}}^2$ inherited from the $(-)$ -component kinematics. As a result, it shows the largest departures from Gaussianity (as reflected by R_G) and a pronounced ellipticity. Moreover, despite the \mathbf{k}_\perp^2 factor in the numerator, the growth of $\mathcal{M}_{\text{BT}}^2$ with k_\perp and angular averaging with $\langle \cos^2 \theta \rangle = 1/2$ dilutes any net enhancement. Together with the rapid Gaussian falloff of f_1^q , this yields the smallest low-order transverse moments for f_4^q in our calculation.

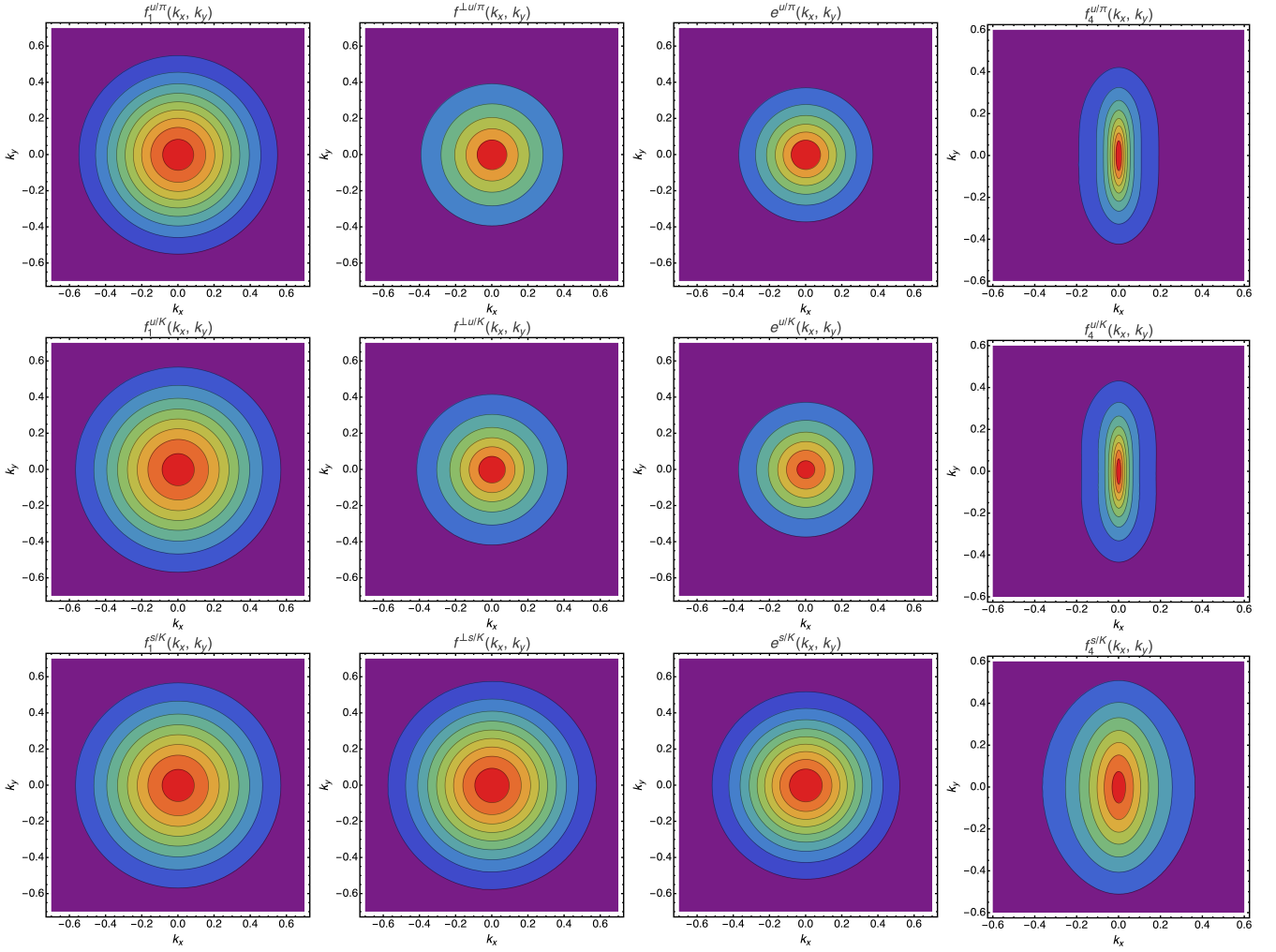


FIG. 6. Transverse profile of u -quark for π^+ (top) and K^+ (middle) as well as the s -quark densities for K^+ (bottom) for the four TMDs obtained from the BT-based LFQM.

The quark transverse-momentum profiles $f^q(\mathbf{k}_\perp)$ in (k_x, k_y) plane are shown in Fig. 6 for the u quark in π^+ (top), the u quark in K^+ (middle), and the s quark in K^+ (bottom). For f_1^q , $f^{\perp q}$, and e^q , the profiles are azimuthally symmetric in (k_x, k_y) and peak sharply at $\mathbf{k}_\perp = \mathbf{0}$, reflecting the underlying Gaussian LFWF. While the twist-2 profile $f_1^{s/K}(\mathbf{k}_\perp)$ is identical to the u -quark profile in K^+ (both are purely Gaussian with the common width $\beta_{q\bar{s}}$), the higher-twist profiles ($f^{\perp s/K}$, $e^{s/K}$, $f_4^{s/K}$) in K^+ exhibit larger RMS widths than their u -quark counterparts. This reflects flavor-dependent kinematic factors in the twist-3 and twist-4 projectors (e.g., m_q/M_0 and $(\mathbf{k}_\perp^2 + m_q^2)/\mathcal{M}_{\text{BT}}^2$). Furthermore, the twist-4 profile $f_4^{q/K}$ shows an elliptic deformation—compressed along k_x and elongated along k_y —stemming from the explicit k_x dependence in $\mathcal{M}_{\text{BT}}^2$ for the $(-)$ -component kinematics. This integrand-level breaking of rotational symmetry distorts the f_4^q contours and, after angular averaging in the \mathbf{k}_\perp integration, further suppresses its radial moments relative to expecta-

tions based on a purely Gaussian f_1^q .

B. PDFs and Longitudinal Moments

Figure 7 shows the twist-2, twist-3, and twist-4 PDFs $f_1^q(x)$, $f^{\perp q}(x)$, $e^q(x)$, and $f_4^q(x)$ for the u - and s -quark sectors in the π^+ and K^+ mesons. The upper panels compare the u -quark distributions in K^+ (solid lines) and π^+ (dashed lines), while the lower panels show the s -quark distributions in K^+ .

For twist-2, the pion distribution $f_1^{u/\pi^+}(x)$ is symmetric in x , reflecting SU(2) flavor symmetry. In K^+ , explicit SU(3) breaking shifts strength such that $f_1^{s/K^+}(x)$ peaks at larger x , while $f_1^{u/K^+}(x)$ is skewed toward smaller x . For higher twists, the u -quark distributions in both π^+ and K^+ remain skewed toward small x . In K^+ , the s -quark higher-twist PDFs are broader and shifted to larger x than the u -quark ones, though their

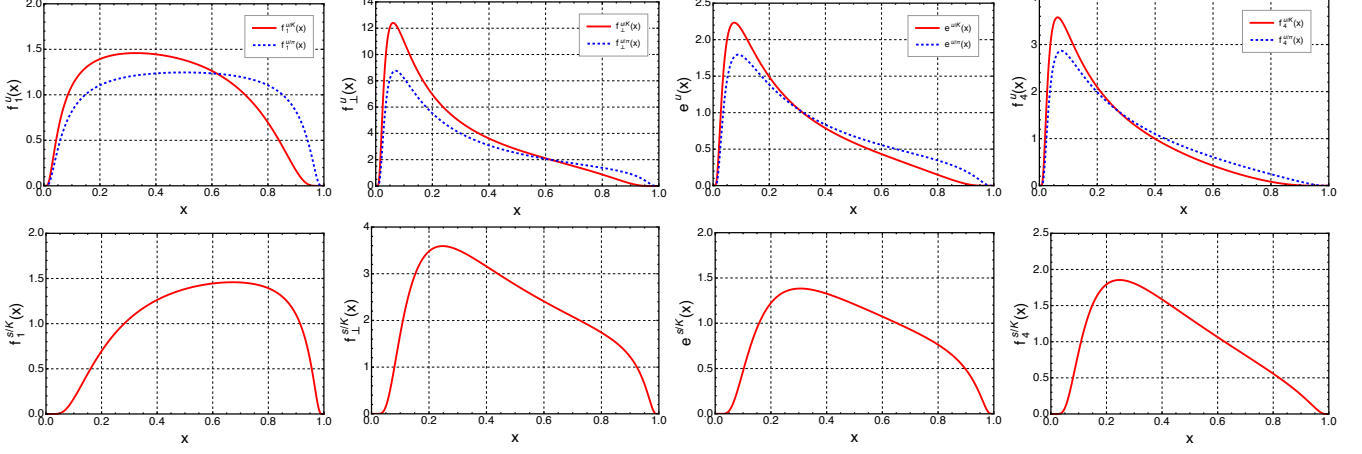


FIG. 7. The u -quark PDFs ($f_1^u, f_1^{\perp u}, e^u, f_4^u$) (top row) for the π^+ (dashed lines) and K^+ (solid lines), and the s -quark PDFs ($f_1^s, f_1^{\perp s}, e^s, f_4^s$) (bottom row) for the K^+ .

peaks still lie below $x = \frac{1}{2}$. As $x \rightarrow 1$, the s -quark tails become comparatively stronger, consistent with explicit m_q -dependent kinematic factors (e.g. m_q/M_0 and $(\mathbf{k}_\perp^2 + m_q^2)/\mathcal{M}_{\text{BT}}^2$) that bias the s channel toward larger x , countered by endpoint suppression from $M_0^2 \propto (1-x)^{-1}$.

A distinct small- x feature appears for the twist-3 transverse distribution. In our fBT-LFQM one has pointwise relation $x f^{\perp q}(x, \mathbf{k}_\perp) = f_1^q(x, \mathbf{k}_\perp)$, which implies $f^{\perp q}(x) = f_1^q(x)/x$ after integrating over \mathbf{k}_\perp . Hence $f^{\perp q}(x)$ is universally enhanced at small x relative to $f_1^q(x)$, while its large- x falloff follows that of f_1^q . Overall, these trends illustrate how mass asymmetries and higher-twist dynamics jointly shape the partonic structure of light pseudoscalar mesons.

In summary, Fig. 7 reveals two robust trends. (i) For the u -quark, the higher-twist PDFs $f_1^{\perp u}(x)$, $e^u(x)$, and $f_4^u(x)$ are more enhanced as $x \rightarrow 0$ and more suppressed as $x \rightarrow 1$ than the leading-twist $f_1^u(x)$. (ii) For the s -quark in K^+ , all three higher-twist PDFs are comparatively suppressed at small x but enhanced as $x \rightarrow 1$ relative to the corresponding u -quark PDFs, consistent with the heavier s mass entering kinematic factors that bias the s channel toward larger x .

We also note that, in our fBT-LFQM, the twist-4 PDF $f_4^q(x)$ satisfies the sum rule in Eq. (51), whereas the pBT-LFQM does not when LF zero-mode contributions are omitted. Likewise, the twist-3 PDF $e^q(x)$ differs between the two formulations due to the treatment of the meson mass in the Lorentz prefactor: the pBT-LFQM uses the physical mass M , while the fBT-LFQM implements the BT replacement $M \rightarrow M_0$ consistently under the (x, \mathbf{k}_\perp) integral.

In particular, the twist-3 PDF $e^q(x)$ obtained from the

fBT-LFQM (pBT-LFQM) yields

$$\begin{aligned} \int_0^1 dx e^{u/\pi^+}(x) &= 0.752 \quad (4.883), \\ \int_0^1 dx e^{u/K^+}(x) &= 0.737 \quad (1.639), \\ \int_0^1 dx e^{s/K^+}(x) &= 0.885 \quad (2.003). \end{aligned} \quad (63)$$

These sizable discrepancies between the fBT- and pBT-LFQMs mirror the qualitative differences also seen for the twist-4 PDF $f_4^q(x)$, and are primarily traceable to the missing LF zero-mode contributions in the pBT-LFQM formulation (see the discussion above and Ref. [62]).

C. QCD evolution of twist-2 PDF $f_1^q(x)$

In Table VI, we list the first ($\langle x \rangle$) and inverse ($\langle x^{-1} \rangle$) x -moments of the unpolarized T-even PDFs $f_1^q(x)$, $e^q(x)$, $f^{\perp q}(x)$, and $f_4^q(x)$ for the u quark in π^+ and the u and s quarks in K^+ within the fBT-LFQM. The n th

TABLE VI. First ($\langle x \rangle$) and inverse ($\langle x^{-1} \rangle$) x -moments of the four unpolarized T-even PDFs $f_1^q(x)$, $e^q(x)$, $f^{\perp q}(x)$, and $f_4^q(x)$ for the u quark in π^+ and the u and s quarks in K^+ within the fBT-LFQM.

PDF	$\langle x \rangle^{u/\pi}$	$\langle x \rangle^{u/K}$	$\langle x \rangle^{s/K}$	$\langle x^{-1} \rangle^{u/\pi}$	$\langle x^{-1} \rangle^{u/K}$	$\langle x^{-1} \rangle^{s/K}$
$f_1^q(x)$	0.5	0.430	0.571	3.108	3.679	2.199
$e^q(x)$	0.255	0.201	0.419	4.325	5.184	2.534
$f^{\perp q}(x)$	1	1	1	20.597	28.638	6.845
$f_4^q(x)$	0.290	0.241	0.417	6.795	8.208	3.327

TABLE VII. Mellin moments of the valence quark PDF in the kaon, $f_1^q(x)$, evaluated at $\mu^2 = 16$ and 27 GeV^2 , respectively. Our results are compared with other available calculations [16, 95, 96], including lattice QCD result using reconstructed PDFs [52].

	$\mu^2 [\text{GeV}^2]$	$\langle x \rangle_{\text{val}}^{u/K}$	$\langle x^2 \rangle_{\text{val}}^{u/K}$	$\langle x^3 \rangle_{\text{val}}^{u/K}$	$\langle x^4 \rangle_{\text{val}}^{u/K}$	$\langle x \rangle_{\text{val}}^{s/K}$	$\langle x^2 \rangle_{\text{val}}^{s/K}$	$\langle x^3 \rangle_{\text{val}}^{s/K}$	$\langle x^4 \rangle_{\text{val}}^{s/K}$
This work	16	0.213	0.080	0.038	0.021	0.282	0.129	0.072	0.044
	27	0.204	0.075	0.036	0.019	0.271	0.121	0.066	0.041
Chen [95]	27	0.28	0.11	0.048		0.36	0.17	0.092	
Watanabe [96]		0.23	0.091	0.045		0.24	0.096	0.049	
BLFQ-NJL [16]		0.201	0.077	0.037	0.021	0.228	0.094	0.049	0.029
Alexandrou [52]		0.217	0.079	0.036	0.019	0.279	0.115	0.058	0.033

moment of a PDF $f^q(x)$ is defined as

$$\langle x^n \rangle^q = \int_0^1 dx x^n f^q(x). \quad (64)$$

We note that the first moment of the twist-3 PDF $f^{\perp q}(x)$ satisfies $\langle x \rangle_{f^\perp}^q = 1$ for any quark flavor. This follows from the TMD relation $xf^{\perp q}(x, \mathbf{k}_\perp) = f_1^q(x, \mathbf{k}_\perp)$ given by Eq. (46), together with the number sum rule for the twist-2 PDF $f_1^q(x)$ given by Eq. (47).

The inverse moment ($n = -1$) is to be understood with convergence controlled by the small- x behavior [27, 28, 97] and represent the regulated Weisberger-type $1/x$ integral. Through the Weisberger relation [98], the flavor-summed and regulated $1/x$ moment is related to $\partial M_H^2 / \partial m_q^2$, which connects high-energy parton structure to low-energy sigma-term physics. In our fBT-LFQM these moments remain finite, whereas in full QCD they require appropriate small- x regularization. From Table VI one sees that in the kaon the s -quark has a larger first moment than the u -quark, while its inverse moment is smaller. This pattern reflects a harder s -quark distribution that is shifted to larger x and depleted at very small x . The shift raises $\langle x \rangle$ but reduces the weight in the $1/x$ -enhanced region, which lowers $\langle x^{-1} \rangle$ relative to u .

The valence PDFs at the model scale μ_0 are evolved to higher scales μ using perturbative QCD. We perform the NNLO DGLAP evolution [99–101] using the HOPPET package [102], which resums the leading logarithms $\ln(\mu^2/\mu_0^2)$ and consistently generates gluon and sea-quark distributions from a valence input through $q \rightarrow qg$, $g \rightarrow (q\bar{q}, gg)$ splittings. Consequently, a structure that is purely valence at μ_0 acquires the expected QCD radiative content at higher μ .

The LFQM transverse scale reflects the intrinsic non-perturbative width of the wave function. We characterize it either by a cutoff k_\perp^{\max} that saturates the TMD integral or by the RMS width $\sqrt{\langle \mathbf{k}_\perp^2 \rangle} = \beta$ of our Gaussian LFWF. By contrast, the collinear scale μ_0 plays the role of a factorization scale that assigns radiation above μ_0 to DGLAP evolution. Our matching strategy is pragmatic. First, for TMDs we choose k_\perp^{\max} so the intrinsic integral

is numerically saturated. In our model this occurs near 1 GeV , which controls TMD plots and transverse moments. Second, for collinear evolution we adopt a lower hadronic input scale $\mu_0 = 0.6 \text{ GeV}$. This provides a clean valence-only starting point, avoids double counting of nonperturbative high- k_\perp strength, and allows us to anchor to phenomenology at $\mu = 2 \text{ GeV}$, for example a pion valence momentum fraction near one half [103–108]. It is also consistent with dynamical PDF setups that start from a low scale with only valence degrees of freedom.

It is reasonable to choose μ_0 of order $\sqrt{\langle \mathbf{k}_\perp^2 \rangle}$. With $\beta \simeq 0.37\text{--}0.39 \text{ GeV}$, the choice $\mu_0 = 0.6 \text{ GeV}$ lies above the intrinsic width yet remains hadronic, while $k_\perp^{\max} \approx 1 \text{ GeV}$ ensures numerical saturation of the TMD integral. The k_\perp -saturation criterion for TMDs is conceptually different from the collinear factorization scale in DGLAP: the former ensures completeness of the intrinsic transverse profile, whereas the latter governs how much strength is generated perturbatively.

Applying this setup ($\mu_0 = 0.6 \text{ GeV}$, $\alpha_s(\mu_0) = 1$) in the DGLAP evolution, we obtain for the pion the first moment of valence-quark PDF at $\mu^2 = 4 \text{ GeV}^2$ as

$$\langle x \rangle_{\text{val}}^\pi \equiv 2\langle x \rangle_{\text{val}}^{u/\pi} = 2 \int_0^1 dx x f_1^{u/\pi}(x) = 0.561. \quad (65)$$

In our model, the valence quarks in the pion carry about 56% of the total momentum at $\mu = 2 \text{ GeV}$, making them the dominant component. The remaining fraction is shared by gluons and sea quarks, in reasonable agreement with recent lattice QCD result [54]. The same evolution setup is applied to the kaon.

Table VII summarizes the lowest four Mellin moments of the kaon's twist-2 u - and s -quark PDFs evaluated at $\mu^2 = 16$ and 27 GeV^2 , and compares them with other theoretical results quoted at 27 GeV^2 [16, 95, 96]. QCD evolution redistributes momentum from valence quarks to gluons and sea quarks. Accordingly, the valence-quark moments decrease as μ^2 increases, while the total momentum is conserved. Overall, our results provide a coherent description of the kaon's valence structure and exhibit systematic trends that show some differences from other theoretical approaches.

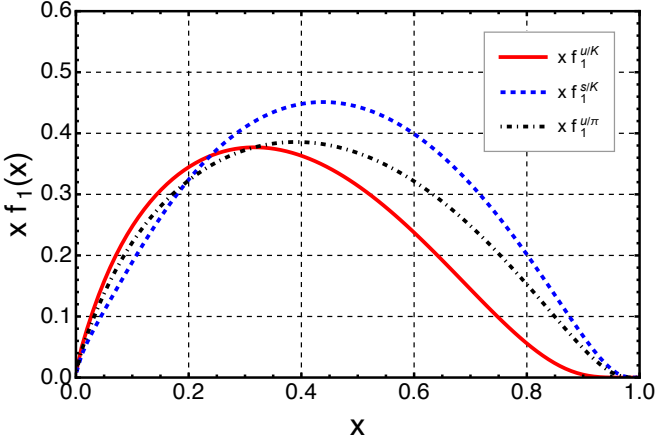


FIG. 8. Valence quark PDFs of the kaon and pion at $\mu^2 = 16 \text{ GeV}^2$, obtained from NNLO evolution starting at $\mu_0 = 0.6 \text{ GeV}$ with $\alpha_s(\mu_0) = 1$.

Figure 8 shows the valence PDFs of the kaon and pion at $\mu^2 = 16 \text{ GeV}^2$. The kaon u -valence distribution is shown as a solid curve, the kaon \bar{s} -valence distribution as a dashed curve, and the pion u -valence distribution as a dash-dotted curve. The pion u -valence PDF is compatible with the experimental constraints of Refs. [109, 110]. For the kaon, the magnitudes and relative behavior of the u - and \bar{s} -valence PDFs are broadly consistent with lattice QCD trends [52–54] as well as recent global QCD analysis [111].

Figure 9 separately shows the gluon PDFs of the kaon and pion at $\mu^2 = 16 \text{ GeV}^2$. The first moments are

$$\langle x \rangle^{g/K} = 0.393, \quad \langle x \rangle^{g/\pi} = 0.590. \quad (66)$$

Thus, in our setup the pion carries a larger gluon momentum fraction than the kaon at this scale. This pattern can follow from starting the evolution at a low hadronic scale with valence-only inputs and from differences in the initial valence shapes: the heavier strange quark tends to retain more longitudinal momentum in the kaon's valence sector, leaving less phase space for gluon radiation as the scale increases. Consequently, the relative gluon sharing reflects both the nonperturbative input at μ_0 and the subsequent DGLAP evolution.

VI. SUMMARY

We have presented a self-consistent fBT-LFQM for the kaon, built on the BT construction, and applied it to the EM form factor, the scalar form factor, and the full set of unpolarized T-even TMDs and their collinear PDFs. We also analyzed the pion's scalar form factor and the associated twist-3 TMD and PDF—topics not covered in our previous work [62]. The defining feature of the fBT-LFQM is the uniform use of the invariant mass M_0 in both the hadronic matrix elements and the

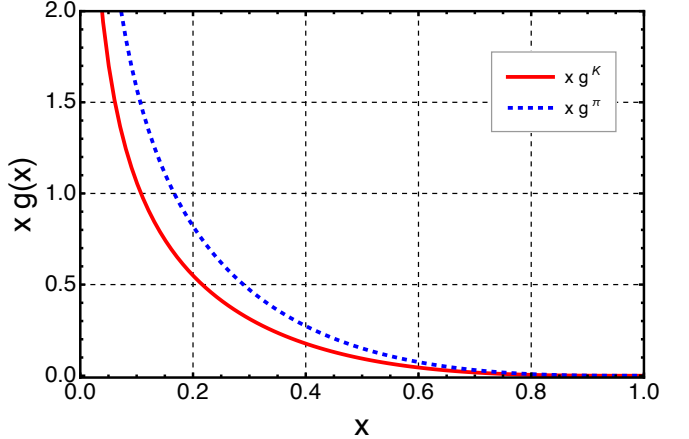


FIG. 9. Gluon PDFs of the kaon and pion at $\mu^2 = 16 \text{ GeV}^2$, obtained from NNLO evolution starting at $\mu_0 = 0.6 \text{ GeV}$ with $\alpha_s(\mu_0) = 1$.

Lorentz prefactors, which enforces four-momentum conservation at the meson-quark vertex and yields current-component-independent extractions of observables.

The fBT-LFQM produces a single, component-independent kaon EM form factor $F_{K^+}(Q^2)$ from the $\Gamma = \gamma^+, \gamma^\perp$, and γ^- projections, and it satisfies charge normalization at $Q^2 = 0$. By contrast, in the pBT-LFQM the γ^+ and γ^\perp extractions agree, but the γ^- channel is contaminated by LF zero modes unless the zero-mode contribution is included explicitly. In the fBT-LFQM, implementing $M \rightarrow M_0$ at the integrand level removes this mismatch and, in practice, resolves the LF zero-mode issue.

We also analyzed the scalar channel in two standard conventions: (A) a direct, no-prefactor definition $f_S(Q^2)$ with $\langle P'|\bar{q}q|P \rangle_{\text{BT}} = f_S(Q^2)$, and (B) a mass-factored definition $F_S(Q^2)$ with $\langle P'|\bar{q}q|P \rangle_{\text{BT}} = 2M f_S(Q^2)$. In the pBT-LFQM these are trivially related, $f_S = 2M f_S$. However, in the fBT-LFQM they are not interchangeable, because the replacement $M \rightarrow M_0(x, \mathbf{k}_\perp)$ must be implemented inside the integrand. The same consistency requirement fixes the normalization of the twist-3 TMD $e^q(x, \mathbf{k}_\perp)$ obtained from the scalar projection. Numerically, we find $F_S^{\text{fBT}}(0) < 1$, whereas the pBT-LFQM extraction yields a value well above unity. This qualitative pattern mirrors the behavior of the EM form factor extracted from the minus component in the pBT-LFQM, where sensitivity to LF zero modes leads to an overestimate at low Q^2 .

We then investigated the T-even TMDs and PDFs obtained from the forward limits of the EM and scalar form factors. The twist-2 TMD $f_1^q(x, \mathbf{k}_\perp)$, which yields the valence-quark PDF, exhibits exact $\text{SO}(2)$ symmetry and a Gaussian \mathbf{k}_\perp profile with an RMS width fixed by the LFWF parameter β_{qQ} , corresponding to an exact Gaussianity ratio $R_G = 1$. The higher-twist TMDs $f^{\perp q}$, e^q , and f_4^q display systematic twist and flavor dependencies, including broader widths for the s quark in K^+ and an el-

lptic deformation of f_4^q induced by the minus component kinematics. In the fBT-LFQM, the twist-4 PDF $f_4^q(x)$ satisfies its forward-limit sum rule, whereas the pBT-LFQM violates it unless the zero-mode contribution is explicitly included. This also implies that the elliptic deformation of f_4^q —a purely dynamical feature arising from the LF kinematic—cannot be captured in the pBT-LFQM approach. Likewise, the twist-3 PDF $e^q(x)$ obtained from the forward limit of scalar form factor $F_S(Q^2)$ exhibits a significantly different normalization between the fBT- and pBT-LFQMs, highlighting how consistent treatment of the invariant mass M_0 inside the integrand ensures proper current conservation and self-consistency of scalar observables.

For collinear NNLO DGLAP evolution, we start from a lower hadronic input scale $\mu_0 = 0.6$ GeV, which provides a clean valence-only baseline while assigning the higher- k_\perp strength above μ_0 to perturbative generation through QCD radiation. This separation ensures that nonperturbative structure is encoded in the initial LFWF, whereas gluon and sea components are dynamically produced by evolution. The parameters μ_0 and $\alpha_s(\mu_0)$ are fixed by anchoring to the empirical pion valence-momentum fraction at $\mu = 2$ GeV, which ensures consistency with global fits. The same setup is then applied to the kaon. Within this setup, we find at high scales that the pion carries a larger gluon momentum fraction than the kaon. This follows from starting the evolution at a low hadronic scale with valence-only inputs and from flavor-asymmetric valence shapes. The heavier strange quark in the kaon retains more longitudinal momentum in the valence sector as the scale increases, which leaves less phase space for gluon radiation and thus a smaller gluon share. Conversely, the lighter and more symmetric pion valence distribution radiates more efficiently, so a larger fraction migrates to gluons

with increasing μ . Hence the relative gluon-quark momentum sharing at high scale reflects both the nonperturbative input at μ_0 and the subsequent NNLO DGLAP evolution.

Overall, the fBT-LFQM establishes a self-consistent framework in which EM and scalar form factors, TMDs, and PDFs can be extracted in a current-component-independent manner, free of LF zero-mode ambiguities. It provides a unified link between nonperturbative quark structure at the model scale and perturbative QCD evolution at higher scales. Future extensions include polarized TMDs, generalized (three-point) correlators, and direct comparisons with precision meson data from upcoming EIC experiments.

ACKNOWLEDGMENT

Y. Choi and H.-M. Choi were supported by the National Research Foundation of Korea (NRF) grant funded by the Korea government under Grant No. RS-2025-02634319 (Y. Choi) and RS-2023-NR076506 (H.-M. Choi). A.J.A. is supported by JAEA Postdoctoral Fellowship Program and was partly supported by the RCNP Collaboration Research Network program under project number COREnet 057, as well as by the PUTI Q1 Grant from the University of Indonesia under contract No. NKB-441/UN2.RST/HKP.05.00/2025. C.-R. Ji was supported in part by the U.S. Department of Energy (Grant No. DE-FG02-03ER41260). The National Energy Research Scientific Computing Center (NERSC) supported by the Office of Science of the U.S. Department of Energy under Contract No. DE-AC02-05CH11231 is also acknowledged.

Appendix A: Derivation of Eq. (43)

Starting from the TMD correlator defined at fixed light-front time $z^+ = 0$,

$$\Phi_q^{[\Gamma]}(x, \mathbf{k}_\perp) = \frac{1}{2} \int [d^3z] e^{i\mathbf{k}\cdot\mathbf{z}} \langle P | \bar{q}(0) \Gamma \mathcal{W}(0, z) q(z) | P \rangle \Big|_{z^+=0}, \quad [d^3z] \equiv \frac{dz^- d^2\mathbf{z}_\perp}{2(2\pi)^3}, \quad (A1)$$

we demonstrate that

$$\int dx \int d^2\mathbf{k}_\perp \Phi_q^{[\Gamma]}(x, \mathbf{k}_\perp) = \frac{1}{2P^+} \langle P | \bar{q}(0) \Gamma q(0) | P \rangle. \quad (A2)$$

We use the light-front scalar product

$$\mathbf{a} \cdot \mathbf{b} = \frac{1}{2} (a^+ b^- + a^- b^+) - \mathbf{a}_\perp \cdot \mathbf{b}_\perp, \quad (A3)$$

and identify $k^+ = xP^+$ so that, with $z^+ = 0$,

$$\mathbf{k} \cdot \mathbf{z} = \frac{1}{2} xP^+ z^- - \mathbf{k}_\perp \cdot \mathbf{z}_\perp. \quad (A4)$$

Integrating Eq. (A1) over x and \mathbf{k}_\perp yields

$$\begin{aligned} \int dx \int d^2\mathbf{k}_\perp \Phi_q^{[\Gamma]}(x, \mathbf{k}_\perp) &= \frac{1}{2} \int [d^3z] \underbrace{\int dx e^{i(\frac{1}{2}P^+)x z^-}}_{= \frac{4\pi}{P^+} \delta(z^-)} \underbrace{\int d^2\mathbf{k}_\perp e^{-i\mathbf{k}_\perp \cdot \mathbf{z}_\perp}}_{= (2\pi)^2 \delta^{(2)}(\mathbf{z}_\perp)} \langle P | \bar{q}(0) \Gamma \mathcal{W}(0, z) q(z) | P \rangle \\ &= \frac{1}{2} \frac{1}{2(2\pi)^3} \frac{4\pi}{P^+} (2\pi)^2 \int dz^- d^2\mathbf{z}_\perp \delta(z^-) \delta^{(2)}(\mathbf{z}_\perp) \langle P | \bar{q}(0) \Gamma \mathcal{W}(0, z) q(z) | P \rangle. \end{aligned} \quad (\text{A5})$$

The delta functions set $z^\mu \rightarrow 0$, so the straight Wilson line reduces to the identity, $\mathcal{W}(0, 0) = \mathbf{1}$, and we obtain

$$\int dx \int d^2\mathbf{k}_\perp \Phi_q^{[\Gamma]}(x, \mathbf{k}_\perp) = \frac{1}{2P^+} \langle P | \bar{q}(0) \Gamma q(0) | P \rangle, \quad (\text{A6})$$

which reproduces Eq. (43) in the main text.

[1] H.-M. Choi and C.-R. Ji, Distribution amplitudes and decay constants for (π, K, ρ, K^*) mesons in the light-front quark model, *Phys. Rev. D* **75**, 034019 (2007).

[2] G. S. Bali *et al.*, Light-cone distribution amplitudes of pseudoscalar mesons from lattice QCD, *J. High Energy Phys.* **2019**, 65.

[3] Z.-F. Cui, M. Ding, F. Gao, K. Raya, D. Binosi, L. Chang, C. D. Roberts, J. Rodríguez-Quintero, and S. M. Schmidt, Kaon and pion parton distributions, *Eur. Phys. J. C* **80**, 1064 (2020).

[4] A. Kock and I. Zahed, Pion and kaon distribution amplitudes up to twist-3 in the QCD instanton vacuum, *Phys. Rev. D* **104**, 116028 (2021).

[5] J. Hua *et al.* (Lattice Parton Collaboration), Pion and kaon distribution amplitudes from lattice QCD, *Phys. Rev. Lett.* **129**, 132001 (2022).

[6] H.-M. Choi and C.-R. Ji, Conformal symmetry and pion form factor: Soft and hard contributions, *Phys. Rev. D* **74**, 093010 (2006).

[7] D. Brömmel, M. Diehl, M. Göckeler, P. Hägler, R. Horsley, T. Kaltenbrunner, C. B. King, D. Pleiter, P. E. L. Rakow, A. Schäfer, G. Schierholz, H. Stübgen, and J. M. Zanotti, The pion form factor from lattice QCD with two dynamical flavours, *Eur. Phys. J. C* **51**, 335 (2007).

[8] S.-i. Nam and H.-C. Kim, Electromagnetic form factors of the pion and kaon from the instanton vacuum, *Phys. Rev. D* **77**, 094014 (2008).

[9] H.-M. Choi and C.-R. Ji, Conformal symmetry and pion form factor: Space- and timelike region, *Phys. Rev. D* **77**, 113004 (2008).

[10] R. Frezzotti, V. Lubicz, and S. Simula, Electromagnetic form factor of the pion from twisted-mass lattice QCD at $N_f = 2$, *Phys. Rev. D* **79**, 074506 (2009).

[11] T. Nguyen, A. Bashir, C. D. Roberts, and P. C. Tandy, Pion and kaon valence-quark parton distribution functions, *Phys. Rev. C* **83**, 062201 (2011).

[12] S.-i. Nam, Parton-distribution functions for the pion and kaon in the gauge-invariant nonlocal chiral-quark model, *Phys. Rev. D* **86**, 074005 (2012).

[13] P. T. P. Hutařuk, I. C. Cloet, and A. W. Thomas, Flavor dependence of the pion and kaon form factors and parton distribution functions, *Phys. Rev. C* **94**, 035201 (2016).

[14] A. Watanabe, T. Sawada, and C. W. Kao, Kaon quark distribution functions in the chiral constituent quark model, *Phys. Rev. D* **97**, 074015 (2018).

[15] K. D. Bednar, I. C. Cloet, and P. C. Tandy, Distinguishing Quarks and Gluons in Pion and Kaon Parton Distribution Functions, *Phys. Rev. Lett.* **124**, 042002 (2020).

[16] J. Lan, C. Mondal, S. Jia, X. Zhao, and J. P. Vary, Pion and kaon parton distribution functions from basis light front quantization and QCD evolution, *Phys. Rev. D* **101**, 034024 (2020).

[17] Q. Wu, C. Han, D. Qing, W. Kou, J. Xie, X. Chen, and F. Wang, Pion parton distribution functions with the nonrelativistic constituent quark model, *Nucl. Phys. B* **994**, 116321 (2023).

[18] P. T. P. Hutařuk, Pseudoscalar Meson Parton Distributions Within Gauge-Invariant Nonlocal Chiral Quark Model, *Symmetry* **17**, 971 (2025).

[19] H.-M. Choi, C.-R. Ji, and L. S. Kisslinger, Skewed quark distribution of the pion in the light-front quark model, *Phys. Rev. D* **64**, 093006 (2001).

[20] H.-M. Choi, C.-R. Ji, and L. S. Kisslinger, Continuity of generalized parton distributions for the pion virtual compton scattering, *Phys. Rev. D* **66**, 053011 (2002).

[21] B. Pasquini, M. Pincetti, and S. Boffi, Chiral-odd generalized parton distributions in constituent quark models, *Phys. Rev. D* **72**, 094029 (2005).

[22] J.-W. Chen, H.-W. Lin, and J.-H. Zhang, Pion generalized parton distribution from lattice QCD, *Nucl. Phys. B* **952**, 114940 (2020).

[23] L. Adhikari, C. Mondal, S. Nair, S. Xu, S. Jia, X. Zhao, and J. P. Vary (BLFQ Collaboration), Generalized parton distributions and spin structures of light mesons from a light-front hamiltonian approach, *Phys. Rev. D* **104**, 114019 (2021).

[24] K. Raya, Z.-F. Cui, L. Chang, J.-M. Morgado, C. D. Roberts, and J. Rodríguez-Quintero, Revealing pion and kaon structure via generalised parton distributions, *Chin. Phys. C* **46**, 013105 (2022).

[25] H.-D. Son and P. T. P. Hutzuruk, Generalized parton distributions of the kaon and pion within the nonlocal chiral quark model, *Phys. Rev. D* **111**, 054007 (2025).

[26] X. Luan and Z. Lu, Higher-twist generalized parton distributions of the pion and kaon at zero skewness in the light-cone quark model, *Phys. Rev. D* **110**, 074022 (2024).

[27] C. Lorcé, B. Pasquini, and P. Schweitzer, Unpolarized transverse momentum dependent parton distribution functions beyond leading twist in quark models, *J. High Energy Phys.* **2015**, 103.

[28] C. Lorcé, B. Pasquini, and P. Schweitzer, Transverse pion structure beyond leading twist in constituent models, *Eur. Phys. J. C* **76**, 415 (2016).

[29] S. Puhan, S. Sharma, N. Kaur, N. Kumar, and H. Dahiya, T-even TMDs for the spin-0 pseudo-scalar mesons up to twist-4 using light-front formalism, *J. High Energy Phys.* **2024**, 075.

[30] Z. Zhu, Z. Hu, J. Lan, C. Mondal, X. Zhao, and J. P. Vary (BLFQ), Transverse structure of the pion beyond leading twist with basis light-front quantization, *Phys. Lett. B* **839**, 137808 (2023).

[31] W.-Y. Liu and I. Zahed, Tomography of pions and kaons in the QCD vacuum: Transverse momentum dependent parton distribution functions, *Phys. Rev. D* **112**, 034039 (2025).

[32] S. Arnold, A. Metz, and M. Schlegel, Dilepton production from polarized hadron hadron collisions, *Phys. Rev. D* **79**, 034005 (2009).

[33] M. Diehl, Introduction to GPDs and TMDs, *Eur. Phys. J. A* **52**, 149 (2016).

[34] B. Pasquini, S. Cazzaniga, and S. Boffi, Transverse momentum dependent parton distributions in a light-cone quark model, *Phys. Rev. D* **78**, 034025 (2008).

[35] J. C. Collins and D. E. Soper, Back-to-back jets in QCD, *Nucl. Phys. B* **193**, 381 (1981).

[36] J. C. Collins, D. E. Soper, and G. Sterman, Transverse momentum distribution in Drell-Yan pair and W and Z boson production, *Nucl. Phys. B* **250**, 199 (1985).

[37] P. J. Mulders and R. D. Tangerman, The complete tree-level result up to order $1/Q$ for polarized deep-inelastic leptoproduction, *Nucl. Phys. B* **461**, 197 (1996).

[38] A. Bacchetta, M. Diehl, K. Goeke, A. Metz, P. J. Mulders, and M. Schlegel, Semi-inclusive deep inelastic scattering at small transverse momentum, *J. High Energy Phys.* **2007**, 093.

[39] A. Bacchetta, F. Delcarro, C. Pisano, M. Radici, and A. Signori, Extraction of partonic transverse momentum distributions from semi-inclusive deep-inelastic scattering, Drell-Yan and Z -boson production, *J. High Energy Phys.* **2017**, 081, [Erratum: *J. High Energy Phys.* **2019**, 051].

[40] J. Zhou, F. Yuan, and Z.-T. Liang, Transverse momentum dependent quark distributions and polarized Drell-Yan processes, *Phys. Rev. D* **81**, 054008 (2010).

[41] J. Arrington *et al.*, Revealing the structure of light pseudoscalar mesons at the electron-ion collider, *J. Phys. G* **48**, 075106 (2021).

[42] D. P. Anderle *et al.*, Electron-ion collider in China, *Front. Phys. (Beijing)* **16**, 64701 (2021).

[43] B. Adams *et al.*, Letter of Intent: A New QCD facility at the M2 beam line of the CERN SPS (COMPASS++/AMBER) (2018) [arXiv:1808.00848 \[hep-ex\]](https://arxiv.org/abs/1808.00848).

[44] J. Badier *et al.* (Saclay-CERN-College de France-Ecole Poly-Orsay), Measurement of the K^-/π^- Structure Function Ratio Using the Drell-Yan Process, *Phys. Lett. B* **93**, 354 (1980).

[45] C. Bourrely, F. Buccella, W.-C. Chang, and J.-C. Peng, Extraction of kaon partonic distribution functions from Drell-Yan and J/ψ production data, *Phys. Lett. B* **848**, 138395 (2024).

[46] W.-C. Chang, J.-C. Peng, S. Platchkov, and T. Sawada, Constraining kaon PDFs from Drell-Yan and J/ψ production, *Phys. Lett. B* **855**, 138820 (2024).

[47] W. Detmold, W. Melnitchouk, and A. W. Thomas, Parton distribution functions in the pion from lattice QCD, *Phys. Rev. D* **68**, 034025 (2003).

[48] R. S. Sufian, J. Karpie, C. Egerer, K. Orginos, J.-W. Qiu, and D. G. Richards, Pion Valence Quark Distribution from Matrix Element Calculated in Lattice QCD, *Phys. Rev. D* **99**, 074507 (2019).

[49] Z. Fan and H.-W. Lin, Gluon parton distribution of the pion from lattice QCD, *Phys. Lett. B* **823**, 136778 (2021).

[50] H.-W. Lin, J.-W. Chen, Z. Fan, J.-H. Zhang, and R. Zhang, Valence-Quark Distribution of the Kaon and Pion from Lattice QCD, *Phys. Rev. D* **103**, 014516 (2021).

[51] H.-W. Lin, Mapping parton distributions of hadrons with lattice QCD, *Prog. Part. Nucl. Phys.* **144**, 104177 (2025).

[52] C. Alexandrou, S. Bacchino, I. Cloët, M. Constantinou, K. Hadjyianakou, G. Koutsou, and C. Lauer (ETM), Pion and kaon $\langle x^3 \rangle$ from lattice QCD and PDF reconstruction from Mellin moments, *Phys. Rev. D* **104**, 054504 (2021).

[53] A. Salas-Chavira, Z. Fan, and H.-W. Lin, First glimpse into the kaon gluon parton distribution using lattice QCD, *Phys. Rev. D* **106**, 094510 (2022).

[54] C. Alexandrou *et al.* (Extended Twisted Mass), Quark and Gluon Momentum Fractions in the Pion and in the Kaon, *Phys. Rev. Lett.* **134**, 131902 (2025).

[55] A. NieMiera, W. Good, and H.-W. Lin, Kaon gluon parton distribution and momentum fraction from 2+1+1 lattice QCD with high statistics, *Phys. Rev. D* **112**, 074504 (2025).

[56] G. P. Lepage and S. J. Brodsky, Exclusive processes in perturbative quantum chromodynamics, *Phys. Rev. D* **22**, 2157 (1980).

[57] S. J. Brodsky, H.-C. Pauli, and S. S. Pinsky, Quantum chromodynamics and other field theories on the light cone, *Phys. Rept.* **301**, 299 (1998).

[58] M. Burkhardt, Light-front quantization of the sine-gordon model, *Phys. Rev. D* **47**, 4628 (1993).

[59] H.-M. Choi and C.-R. Ji, Nonvanishing zero modes in the light-front current, *Phys. Rev. D* **58**, 071901 (1998).

[60] B. L. G. Bakker, H.-M. Choi, and C.-R. Ji, Regularizing the divergent structure of light-front currents, *Phys. Rev. D* **63**, 074014 (2001).

[61] H.-M. Choi and C.-R. Ji, Light-front zero-mode contribution to the good current in weak transitions, *Phys. Rev. D* **72**, 013004 (2005).

[62] H.-M. Choi and C.-R. Ji, Consistency of the pion form factor and unpolarized transverse momentum dependent parton distributions beyond leading twist in the light-front quark model, *Phys. Rev. D* **110**, 014006 (2024).

[63] H.-M. Choi and C.-R. Ji, Self-consistent covariant de-

scription of vector meson decay constants and chirality-even quark-antiquark distribution amplitudes up to twist 3 in the light-front quark model, *Phys. Rev. D* **89**, 033011 (2014).

[64] H.-M. Choi and C.-R. Ji, Consistency of the light-front quark model with chiral symmetry in the pseudoscalar meson analysis, *Phys. Rev. D* **91**, 014018 (2015).

[65] H.-M. Choi and C.-R. Ji, Two-particle twist-3 distribution amplitudes of the pion and kaon in the light-front quark model, *Phys. Rev. D* **95**, 056002 (2017).

[66] A. J. Arifi, H.-M. Choi, C.-R. Ji, and Y. Oh, Independence of current components, polarization vectors, and reference frames in the light-front quark model analysis of meson decay constants, *Phys. Rev. D* **107**, 053003 (2023).

[67] A. J. Arifi, H.-M. Choi, and C.-R. Ji, Pseudoscalar meson decay constants and distribution amplitudes up to the twist-4 in the light-front quark model, *Phys. Rev. D* **108**, 013006 (2023).

[68] H.-M. Choi, Self-consistent light-front quark model analysis of $B \rightarrow D\ell\nu_\ell$ transition form factors, *Phys. Rev. D* **103**, 073004 (2021).

[69] Y. Choi, H.-D. Son, and H.-M. Choi, Gravitational form factors of the pion in the self-consistent light-front quark model, *Phys. Rev. D* **112**, 014043 (2025).

[70] M. Ridwan, A. J. Arifi, and T. Mart, Self-consistent $M1$ radiative transitions of excited B_c and heavy quarkonia with different polarizations in the light-front quark model, *Phys. Rev. D* **111**, 016011 (2025).

[71] B. Bakamjian and L. H. Thomas, Relativistic particle dynamics. II, *Phys. Rev.* **92**, 1300 (1953).

[72] W. N. Polyzou, Examining the equivalence of Bakamjian-Thomas mass operators in different forms of dynamics, *Phys. Rev. C* **82**, 064001 (2010).

[73] P. L. Chung, F. Coester, B. D. Keister, and W. N. Polyzou, Hamiltonian light-front dynamics of elastic electron-deuteron scattering, *Phys. Rev. C* **37**, 2000 (1988).

[74] H.-M. Choi and C.-R. Ji, Mixing angles and electromagnetic properties of ground state pseudoscalar and vector meson nonets in the light-cone quark model, *Phys. Rev. D* **59**, 074015 (1999).

[75] H.-M. Choi and C.-R. Ji, Light-front quark model analysis of exclusive $B \rightarrow D\ell\nu_\ell$ semileptonic heavy meson decays, *Phys. Lett. B* **460**, 461 (1999).

[76] H.-M. Choi, C.-R. Ji, Z. Li, and H.-Y. Ryu, Variational analysis of mass spectra and decay constants for ground state pseudoscalar and vector mesons in the light-front quark model, *Phys. Rev. C* **92**, 055203 (2015).

[77] A. J. Arifi, H.-M. Choi, C.-R. Ji, and Y. Oh, Mixing effects on $1S$ and $2S$ state heavy mesons in the light-front quark model, *Phys. Rev. D* **106**, 014009 (2022).

[78] N. Dhiman, H. Dahiya, C.-R. Ji, and H.-M. Choi, Twist-2 pseudoscalar and vector meson distribution amplitudes in light-front quark model with exponential-type confining potential, *Phys. Rev. D* **100**, 014026 (2019).

[79] B. Pandya, B. Gurjar, D. Chakrabarti, H.-M. Choi, and C.-R. Ji, Mixing effects on spectroscopy and partonic observables of heavy mesons with logarithmic confining potential in a light-front quark model, *Phys. Rev. D* **110**, 094021 (2024).

[80] W. Jaus, Relativistic constituent-quark model of electroweak properties of light mesons, *Phys. Rev. D* **44**, 2851 (1991).

[81] W. Jaus, Semileptonic decays of B and D mesons in the light-front formalism, *Phys. Rev. D* **41**, 3394 (1990).

[82] H. J. Melosh, Quarks: Currents and constituents, *Phys. Rev. D* **9**, 1095 (1974).

[83] S. Navas *et al.* (Particle Data Group), Review of particle physics, *Phys. Rev. D* **110**, 030001 (2024).

[84] S. Aoki *et al.* (JLQCD and TWQCD collaborations), Pion form factors from two-flavor lattice QCD with exact chiral symmetry, *Phys. Rev. D* **80**, 034508 (2009).

[85] C. Alexandrou, S. Bacchio, I. Cloët, M. Constantinou, J. Delmar, K. Hadjyianakou, G. Koutsou, C. Lauer, and A. Vaquero (ETM Collaboration), Scalar, vector, and tensor form factors for the pion and kaon from lattice qcd, *Phys. Rev. D* **105**, 054502 (2022).

[86] X. Wang, Z. Xing, J. Kang, K. Raya, and L. Chang, Pion scalar, vector, and tensor form factors from a contact interaction, *Phys. Rev. D* **106**, 054016 (2022).

[87] S. Puhan and H. Dahiya, Scalar, vector, and tensor form factors of pion and kaon, *Phys. Rev. D* **111**, 114039 (2025).

[88] R. Jaffe and X. Ji, Chiral-odd parton distributions and Drell-Yan processes, *Nucl. Phys. B* **375**, 527 (1992).

[89] A. V. Efremov and P. Schweitzer, The chirally-odd twist-3 distribution $e^a(x)$, *J. High Energy Phys.* **2003**, 006.

[90] J. Gasser and H. Leutwyler, Chiral perturbation theory to one loop, *Annals Phys.* **158**, 142 (1984).

[91] A. J. Arifi, H.-M. Choi, and C.-R. Ji, Beyond leading twist: ρ meson decay constants and distribution amplitudes in a self-consistent light-front quark model, *Phys. Rev. D* **112**, 033009 (2025).

[92] S. Boffi, A. V. Efremov, B. Pasquini, and P. Schweitzer, Azimuthal spin asymmetries in light-cone constituent quark models, *Phys. Rev. D* **79**, 094012 (2009).

[93] U. D'Alesio and F. Murgia, Azimuthal and Single Spin Asymmetries in Hard Scattering Processes, *Prog. Part. Nucl. Phys.* **61**, 394 (2008).

[94] P. Schweitzer, T. Teckentrup, and A. Metz, Intrinsic transverse parton momenta in deeply inelastic reactions, *Phys. Rev. D* **81**, 094019 (2010).

[95] C. Chen, L. Chang, C. D. Roberts, S. Wan, and H.-S. Zong, Valence-quark distribution functions in the kaon and pion, *Phys. Rev. D* **93**, 074021 (2016).

[96] A. Watanabe, T. Sawada, and C. W. Kao, Meson cloud effects on kaon quark distribution functions and the SU(3) flavor symmetry, *Nucl. Part. Phys. Proc.* **300-302**, 121 (2018).

[97] S. J. Brodsky, F. J. Llanes-Estrada, and A. P. Szczepaniak, Illuminating the $1/x$ moment of parton distribution functions (2007) p. 149, contribution to MENU 2007, [arXiv:0710.0981 \[nucl-th\]](https://arxiv.org/abs/0710.0981).

[98] W. I. Weisberger, Partons, electromagnetic mass shifts, and the approach to scaling, *Phys. Rev. D* **5**, 2600 (1972).

[99] Y. L. Dokshitzer, Calculation of the structure functions for deep inelastic scattering and e^+e^- annihilation by perturbation theory in quantum chromodynamics, *Sov. Phys. JETP* **46**, 641 (1977).

[100] V. N. Gribov and L. N. Lipatov, Deep inelastic electron scattering in perturbation theory, *Phys. Lett. B* **37**, 78 (1971).

[101] G. Altarelli and G. Parisi, Asymptotic freedom in parton language, *Nucl. Phys. B* **126**, 298 (1977).

[102] G. P. Salam and J. Rojo, A Higher Order Perturbative

Parton Evolution Toolkit (HOPPET), *Comput. Phys. Commun.* **180**, 120 (2009).

[103] S. Boffi, B. Pasquini, and M. Traini, Helicity dependent generalized parton distributions in constituent quark models, *Nucl. Phys. B* **680**, 147 (2004).

[104] B. Pasquini and P. Schweitzer, Pion transverse momentum dependent parton distributions in a light-front constituent approach, and the Boer-Mulders effect in the pion-induced Drell-Yan process, *Phys. Rev. D* **90**, 014050 (2014).

[105] W. Broniowski, E. R. Arriola, and K. Golec-Biernat, Generalized parton distributions of the pion in chiral quark models and their QCD evolution, *Phys. Rev. D* **77**, 034023 (2008).

[106] A. Courtoy and S. Noguera, Enhancement effects in exclusive $\pi\pi$ and $\rho\pi$ production in $\gamma^*\gamma$ scattering, *Phys. Lett. B* **675**, 38 (2009).

[107] P. J. Sutton, A. D. Martin, R. G. Roberts, and W. J. Stirling, Parton distributions for the pion extracted from Drell-Yan and prompt photon experiments, *Phys. Rev. D* **45**, 2349 (1992).

[108] S. Capitani, K. Jansen, M. Papinutto, A. Shindler, C. Urbach, and I. Wetzorke, Parton distribution functions with twisted mass fermions, *Phys. Lett. B* **639**, 520 (2006).

[109] J. S. Conway *et al.* (E615), Experimental Study of Muon Pairs Produced by 252 GeV Pions on Tungsten, *Phys. Rev. D* **39**, 92 (1989).

[110] M. Aicher, A. Schafer, and W. Vogelsang, Soft-gluon resummation and the valence parton distribution function of the pion, *Phys. Rev. Lett.* **105**, 252003 (2010).

[111] P. C. Barry, C.-R. Ji, W. Melnitchouk, N. Sato, and F. Steffens (JAM), First simultaneous global QCD analysis of kaon and pion parton distributions with lattice QCD constraints (2025) [arXiv:2510.11979 \[hep-ph\]](https://arxiv.org/abs/2510.11979).